JGP Journal of General Physiology

ARTICLE

Excitation–Contraction Coupling

Cardiomyocyte ryanodine receptor clusters expand and coalesce after application of isoproterenol

David R.L. Scriven[1], Anne Berit Johnsen[2], Parisa Asghari[1], Keng C. Chou[3], and Edwin D.W. Moore[1]

Earlier work has shown that ventricular ryanodine receptors (RyR2) within a cluster rearrange on phosphorylation as well as with a number of other stimuli. Using dSTORM, we investigated the effects of 300 nmol/liter isoproterenol on RyR2 clusters. In rat ventricular cardiomyocytes, there was a symmetrical enlargement of RyR2 cluster areas, a decrease in the edge-to-edge nearest neighbor distance, and distribution changes that suggested movement to increase the cluster areas by coalescence. The surface area covered by the phosphorylated clusters was significantly greater than in the control cells, as was the cluster density. This latter change was accompanied by a decreased cluster fragmentation, implying that new tetramers were brought into the sarcoplasmic reticulum. We propose a possible mechanism to explain these changes. We also visualized individual RyR2 tetramers and confirmed our earlier electron-tomographic finding that the tetramers are in a disorganized but non-random array occupying about half of the cluster area. Multiclusters, cluster groups defined by the maximum distance between their members, were analyzed for various distances. At 100 nm, the areas occupied by the multiclusters just exceeded those of the single clusters, and more than half of the multiclusters had only a single subcluster that could initiate a spark. Phosphorylation increased the size of the multiclusters, markedly so for distances >100 nm. There was no relationship between the number of subclusters in a group and the area covered by it. We conclude that isoproterenol induces rapid, significant, changes in the molecular architecture of excitation–contraction coupling.

Introduction

Our knowledge of the arrangement and behavior of the cardiac ryanodine receptor (RyR2) has undergone a dramatic transformation in the past decade. Originally it was thought that the arrangement of RyR2 within a dyad followed that of RyR1, the skeletal muscle ryanodine receptor, which appears in large clusters having a regular checkerboard arrangement (Ferguson et al., 1984). Later, it was found that isolated RyR1 in a lipid bilayer would spontaneously arrange in a checkerboard array (Yin and Lai, 2000; Yin et al., 2005), although this checkerboard had an overlap between the tetramers of one-half of a tetramer's length resulting in 75% of the space being occupied by tetramers rather than the 50% of a true checkerboard. Although RyR2 is not amenable to the techniques used by Yin et al. (2005), it was assumed that the RyR2 clusters, were, like RyR1, large, well-ordered, and organized in a static array, and this is how super-resolution data has been interpreted. In the first superresolution study of the RyR2 distribution, Baddeley et al. (2009) used a Yin-Lai checkerboard in their data display but calculated the number of tetramers as if the area of a cluster was 100% filled by 30 × 30 nm tetramers (900 nm^2). This packed array model has been used in nearly all superresolution studies of RyR2 published since then (Hou et al., 2015; Macquaide et al., 2015; Kolstad et al., 2018; Shen et al., 2019). A study using DNA-Paint (Jayasinghe et al., 2018) found a very different distribution of RyR2—most seemed to be separate with the distance between them having a mode of 40 nm with about 33% of the area being occupied by RyR2.

An electron-tomographic study of the distribution of RyR2 in the mouse cardiomyocyte (Hayashi et al., 2009) found that the size of the dyads was extremely diverse, varying 400-fold between the smallest and largest, with the smallest containing as little as one tetramer. Correlation microscopy, using Ca^{2+} spark imaging and electron tomography (Asghari et al., 2014), showed

[1]Department of Cellular and Physiological Sciences, University of British Columbia, Vancouver, Canada; [2]Department of Teacher Education, Norwegian University of Science and Technology, Trondheim, Norway; [3]Department of Chemistry, University of British Columbia, Vancouver, Canada.

Correspondence to Edwin D.W. Moore: edwin.moore@ubc.ca

This work is part of a special issue on excitation–contraction coupling.

that in control rat ventricular myocytes, the arrangement of the tetramers was not uniform but a mixed checkerboard and side-by-side array. In these observations, the tetramer associations were not fixed as in a Yin-Lai checkerboard; a side-by-side arrangement implied that at least 67% of a side was in contact with another tetramer while the checkerboard arrangement had a variable overlap from just touching to two-thirds of a side. Further, they found that the organization of the tetramers varied with treatment, with phosphorylation both increasing the spark frequency and moving the tetramers into a large checkerboard array while high Mg^{2+} reduced the spark frequency and the tetramers clumped into a side-by-side arrangement. The effects of phosphorylation were confirmed in a later study (Asghari et al., 2020), which also found that the immunophilins FKBP12 and 12.6 caused most of the tetramers to be in a side-by-side configuration concomitant with a decrease in the spark frequency. Knowing how fully the tetramers populate the dyad and their arrangement within it is important in understanding spark production, and this has been highlighted both experimentally (Novotová et al., 2020) and with mathematical models (Iaparov et al., 2021).

Using a highly stable home-built superresolution system, we were able to visualize objects with a similar size and shape as individual RyR2 receptors on the surface of the ventricular myocyte. We found that the RyR2 distribution within the clusters was neither a checkerboard nor a rectangular or dispersed array, but was similar to our earlier electron-tomographic finding (Asghari et al., 2014, 2020) that the tetramers form a disordered, though not random, array. Analyzing the structure of RyR2 clusters revealed that between 75% and 90% of the tetramers were in clusters large enough to produce sparks. We analyzed multiclusters (cluster groups defined by the maximum distance between their members) for various distances. We found that the area occupied by multiclusters only exceeded those of singleton clusters at distances of 100 nm and above. At a distance of 100 nm, more than half of the multiclusters had only a single subcluster that could initiate a spark. There was no relationship between the number of subclusters in a multicluster and the area covered by it.

Phosphorylation induced by a physiological concentration of isoproterenol (ISO) caused a symmetrical increase in the cluster areas, with some of the small clusters coalescing. The clusters covered a greater surface area of the cell after phosphorylation and the cluster density increased. This increase was not due to changes in cluster fragmentation but to new tetramers being introduced into the junctional sarcoplasmic reticulum (jSR). We propose a possible mechanism to explain these changes.

Materials and methods

The experiments used ventricular myocytes from adult rats. Animal handling was done in accordance with the guidelines of the Canadian Council on Animal Care and approved by the animal research committee of the University of British Columbia (UBC #A17-0040). All chemicals were purchased from Sigma-Aldrich, unless otherwise stated.

The isolation of live cardiomyocytes has been described elsewhere (Asghari et al., 2014). The base solution used for isolation, restoration of calcium levels, and incubation was Joklik MEM (M0518) supplemented with 23 mmol/liter $NaHCO_3$, 1.2 mmol/liter $MgSO_4$, and 1 mmol/liter DL-carnitine. After isolation, the cells were gradually restored to physiological calcium levels (1.0 mmol/liter), ending in an incubation solution (base plus 1.0 mmol/liter $CaCl_2$). The cells were then split into two groups: the controls in the incubation solution and the rest in a solution to which 300 nmol/liter ISO was added. Both incubations were for 5 min at 37°C. Cells were fixed with 2% paraformaldehyde for 10 min, washed in phosphate-buffered saline (PBS), and settled on poly-L-lysine coated coverslips. The cells were permeabilized with 0.1% TritonX for 10 min, washed with PBS, treated with Image-IT FX signal enhancer (I36933; Life Technologies) for 30 min, washed, and then blocked with BlockAid solution (B10710; Life Technologies) for 1 h. The cells were labeled with 1:100 anti-RyR2 (clone C3-33; 1 mg/ml), kept at 4°C overnight, and then washed and labeled with 1:100 anti-mouse Alexa 647 (Life Technologies), after which they were washed and fixed again using the same protocol. A low concentration of 100 nm tracking beads (F8799; Life Technologies) was added to the coverslips and allowed to settle overnight. Imaging was performed in a standard GLOX-thiol solution (a nitrogenated TN buffer [50 mmol/l Tris, 10 mmol/liter NaCl, pH 8.0], 0.5 mg/ml glucose oxidase, 40 mg/ml catalase, 10% [wt/vol] glucose, and 140 mmol/liter 2-mercaptoethanol). The coverslip with the attached cardiomyocytes was mounted onto a chamber with a volume of 700 µl, which was filled with the imaging solution and sealed. Blinks were collected from the surface of the myocyte with the laser beam adjusted to near-TIRF incidence.

Cells came from four randomly chosen mature male Wistar rats weighing between 200 and 250 g. Images were obtained from the surfaces of 21 control and 20 ISO-treated cells. 24 control segments covered a total area of 2,210.3 μm^2 while the 23 ISO-treated segments covered 1,327.8 μm^2.

The software driving the position of the imaging stage of the custom-built microscope (Tafteh et al., 2016) was updated to provide greater stability with ΔX and $\Delta Y < 0.6$ nm RMS and $\Delta Z < 2.0$ nm RMS; a plot showing the stage stability over the course of an experiment is shown in Fig. S1 A. Blinks were collected from images within a 50 × 50 µm window and the lateral positions (X and Y) of fluorophores were determined by fitting each fluorescent peak with an elliptical error function (Huang et al., 2011) and were filtered by removing blinks with an estimated uncertainty in their XY position >10 nm, Z position >40 nm, and a goodness of fit <0.9. On average, this excluded 20% of the captured blinks. A histogram of the uncertainties in the positions of 2.6 million control data blinks that satisfied the above criteria is shown in Fig. S1 B. The positions were stored as floating-point numbers but rounded to the nearest nanometer. For display, each blink was defined as a 1 nm^2 block. Given the precision and accuracy of our system in the XY plane and noting that the possible error in Z is larger than the dimensions of the tetramer turret section (Van Petegem, 2015), we should be able to obtain images of single tetramers, provided that their tops face the

camera. For this reason, we restricted our images to those that showed the peripheral couplings on the surface of the cardiomyocyte. Even with this restriction, the actual distance between the blink-producing fluorophore and the target protein depends on the nature of the labeling. In our case, with primary–secondary labeling and viewing the tetramers from above, the fluorophores can appear to be between 0 and 15 nm distant from the RyR2 tetramer to which they are attached. After acquisition and filtering, we rotated the image in 3-D, kept those surface areas that were parallel to the XY plane, removed any subsurface signal, and collapsed the Z axis, which resulted in a 2-D image representing a layer of blinks about 100 nm thick.

Tetramer placement

A sample image (Fig. 1 A) shows that the blinks define clusters with areas of density within them. On magnification of the image, we noted that many of the densities were the approximate size and shape of a single RyR2. We then manually placed squares of the appropriate size, orientation, and position onto those images to illustrate our finding. We were unable to automate this process because we could not always make out where the tetramers were and could not develop criteria that gave consistent results. This was probably due to blinks with poor localization producing noisy data as well as operating at the very limit of what is possible with superresolution imaging. The images with the squares representing tetramers are our best guess of the tetramer placement within the clusters we examined.

Cluster analysis

We first prepared the image for a Delaunay triangulation by creating a data structure in which the number of blinks at each XY coordinate and the coordinate were linked but separated. To identify the clusters, we performed a Delaunay triangulation on the coordinate data and then culled the connections longer than a given length. This length, which we call the neighborhood limit, was initially set at 30 nm close to the width of a tetramer; this defined the base clusters for an image. We investigated values of 40, 50, 60, and 80 nm, with the 60 nm value being close to the maximum distance between tetramers observed in the tomography data of Asghari et al. (2012; 2020). We also investigated the properties of clusters that satisfied calcium release unit (CRU) models with limits of 100 nm (Sobie et al., 2006) and 150 nm (Macquaide et al., 2015).

We made two assumptions in our analysis: that the majority of the blinks were coming from fluorophores associated with the receptors and that blink density would be highest near and on the receptors. To identify the tetramers, we then examined the density of blinks using a modification of a method for 2-D astronomical images (Cautun and van de Weygaert, 2011 *Preprint*). We sum the areas of the Delaunay triangles connected to a point (Fig. S2) and use the reciprocal to calculate the density.

$$\text{Blink density} = k * \frac{b}{A}$$

where k = 3, scaling factor; b = number of blinks per point; and A = summed Delaunay area. This calculation is done before the edges in the triangulation are culled so that each point has an accurate density.

A plot of the density (Fig. S2 B i) shows a sharp decay making it difficult to discriminate between the background and signal from the tetramers. A log transformation of the data (Fig. S2 B ii) produces a distribution that is almost normal in shape with an additional tail that is mostly noise. Most of this noise was removed by the filters described below. The average blink density in the clusters was used to set a threshold for images so that the isolated tetramers were well-defined. The density threshold, expressed as the $\log_{10}$(density), was used as an imaging tool to enhance the contrast between areas of high and low blink density but did not alter the data.

Analysis program

Blink data was analyzed using a two-step process. First, the objects within each cluster defined by a neighborhood limit of 30 nm were identified and low-density clusters with fewer than six blinks were excluded. This removed the necessity of doing a separate nearest-neighbor search to exclude isolated blinks. The remaining clusters were fitted using α shapes (Bernardini and Bajaj, 1997), and their areas were calculated (less any large holes in their interiors; Fig. S3 A). This allowed us to exclude clusters smaller than a single tetramer (<600 nm^2). The best value for the α parameter was 700, which produced a perimeter that conformed to the surface, avoiding small clefts, while also identifying large holes in the interior. We examined other values of the α parameter and found that indentations and the roughness of the cluster edge was the major determinant of the accuracy of the fit and thus the area calculations. Rarely (1 in 600 clusters), the fit failed and the α parameter was automatically increased until the fit succeeded. Clusters with an area <2,000 nm^2 were also fitted with a minimum ellipse to ensure that the minor axis was at least 24.5 nm so as to exclude blink clusters too thin to encompass a tetramer. The clusters that satisfied these criteria provided base data for all subsequent analyses.

On the second pass, for neighborhood limits >30 nm, a Delaunay triangulation was performed on the base data and we calculated the convex hulls that surrounded each cluster. These hulls were then populated with the clusters identified from the first pass by determining whether the cluster centroid fell inside the hull. For each cluster, the area was the sum of the area of the individual subclusters. Using this methodology, the total cluster area within an image remained constant irrespective of the neighborhood limit and we could capture the area of each subcluster within a cluster. These steps were skipped for the 30-nm neighborhood limit. We then characterized the cluster properties. The median of the summed areas was estimated from an integral of the areas with a step size of 100 nm. Each cluster, defined by a convex hull, was fitted with a minimum ellipse (Gärtner and Schönherr, 1998), described by the general equation, which was then converted into the major and minor axes lengths giving a rough measure of the cluster's width, breadth, and eccentricity (Fig. S3 B). The algorithm for fitting the ellipse is very slow (scaling as n) when fitting clusters with large numbers of points, and we found that using the coordinates generated from the convex hull rather than all the cluster data

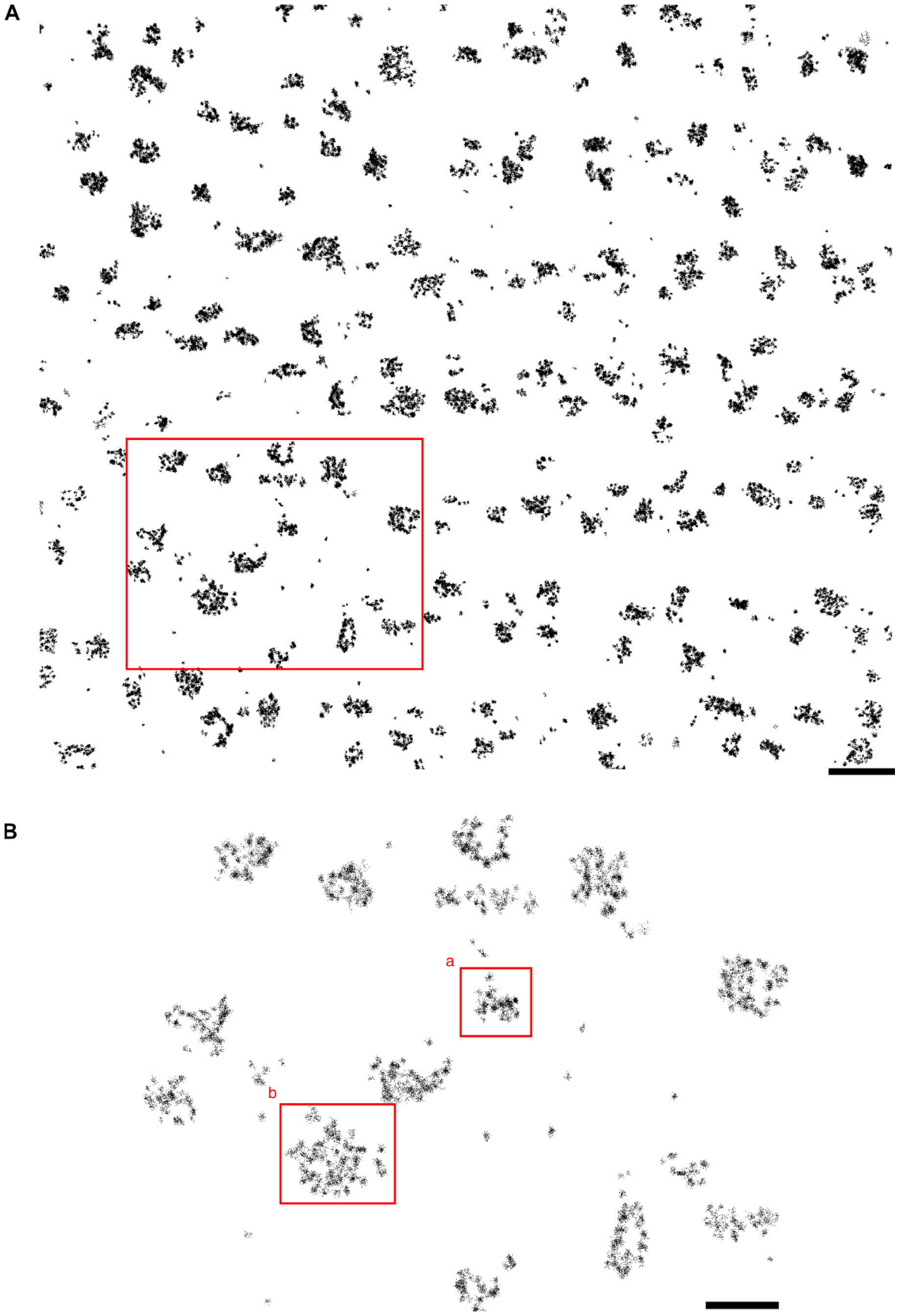

Figure 1. **Blink distribution on the surface of a cardiomyocyte. (A)** Blink data showing tetramer clusters on the surface of a cardiomyocyte. Area is 13.0 × 11.8 µm. Z lines run left to right and are about 1.75 µm apart. Scale bar: 1 µm. The cluster structure and, in some cases, individual tetramers are clearly visible with a twofold zoom. **(B)** Enlargement of the section in A outlined in red. Densities and the size of tetramers can be seen throughout the image. Scale bar: 1 µm.

points produced very rapid and identical results. Lastly, we calculated the edge-to-edge nearest neighbor distances between the clusters. The geometrical analysis (α shapes, nearest neighbors, convex hulls, and minimum ellipses) was done using algorithms from the Computational Graphics Algorithmic Library (http://cgal.org) in a C++ program written by the first author. All calculations were performed using 8-byte floating point numbers. The program has two optional outputs; one listing the characteristics of each cluster in the image and the other listing the blinks in the clusters that remained after the image was processed, with the log density given for each blink. This latter data set was used for calculations of the image resolution using the NanoJ-SQUIRREL implementation of the Fourier ring correlation (FRC; Culley et al., 2018) and was not used in image display or any other analysis. All images were created with the Okabe-Ito color palette to accommodate the color blind (Wong, 2011), and the color names used in this paper correspond to those listed in Fig. 2 of that paper.

Statistics

All of the measurements (cluster areas, hull areas, ellipse axes, etc.) produced non-normal distributions that could not be transformed into normality, so all the statistics we used were based on ranks. We report means for comparison but do not report standard errors for non-normal data. We pooled all the data in each treatment group. For clarity, we present the distributions as cumulative data functions (CDF) that display the distribution as a monotonic increasing curve. To determine whether the differences between control and ISO-treated cells were significant, we analyzed the distributions using the Anderson–Darling test (Scholz and Stephens, 1987) and also compared the medians of the data sets using the Mann–Whitney test. The results we report are the larger of the two probabilities calculated. For multiple comparisons, we used the Holm–Bonferroni test (Holm, 1979) with $\alpha = 0.05$. Heteroscedasticity was tested using the Breusch–Pagan test (Breusch and Pagan, 1979). Cluster data analysis and the associated graphs and tables were done using MATLAB and R.

Online supplemental material

Fig. S1 shows the stability of the X, Y, and Z axes of the piezoelectric stage for the duration of a single image acquisition as well as the maximum errors in X, Y, and Z of blink placement. Fig. S2 uses a Delaunay triangulation to show how the blink density is calculated and displays the blink density of a large data set in both in linear and logarithmic forms. Fig. S3 displays the α-shape generated boundaries and the minimum ellipses of each cluster in Fig. 1 B. Fig. S4 shows clusters and tetramers on the surface of three different control cells. Fig. S5 presents blink data showing the effect of ISO on the surface distribution of clusters in two different cells.

Results

Locating the tetramers

Fig. 1 A shows blinks from a large area (147.9 μm^2) on the surface of a control cardiomyocyte. The diversity of cluster shapes and sizes is such that there is no "typical" cluster. A few of the clusters have holes or a crescent shape, surrounding a region where there are no RyR2, which may be a t-tubule, although these are relatively rare. The sarcomeres are about 1.8 μm apart, with the clusters placed on either side of the Z lines. There are 300,809 blinks in this image at 292,275 different points (XY coordinates), giving an average of 1.03 blinks per point; the blink density is 2,030 blinks/μm^2. At full magnification, most illuminated pixels contain more than one blink. Inspection of the image shows that while there are clusters containing well-defined densities, there are others in which there is no clear pattern. This is reflected in variations in the image resolution (Culley et al., 2018) with a mean of 28.1 nm with a range of 21.6–35.6 nm. A threefold magnification of the area in Fig. 1 A outlined in red is shown in Fig. 1 B. At this magnification, multiple densities can be seen inside the clusters, in some cases producing objects in the shape of tetramers. The blink densities of the individual clusters are high, with only two having a value <20,000/μm^2. The two clusters outlined in red are further analyzed in Fig. 2.

The first image (Fig. 2, A i and B i) for both clusters shows the blink data after first-pass filters have been applied. For clarity, the blinks in Fig. 2 are represented by a 2 × 2 pixel block. The blink density of Fig. 2 A is high, 35,877/μm^2, while in Fig. 2 B it is 22,007/μm^2, typical of the rest of the clusters The highest blink densities are associated with the labeled RyR2, and the second image of each cluster (Fig. 2, A ii and B ii) shows the cluster encoded for density; those below the density threshold of −1.6 are shown in sky blue, while those equal and above are in vermillion. In both images, there are clearly defined, high-density, square objects. Applying this threshold also increases the resolution of Fig. 1 B to 20.9 nm with a range of 9.5–28.0 nm. In both images there are isolated rectangular blocks—two in the top cluster (Fig. 2 A ii) and four in the lower cluster (Fig. 2 B ii). When a RyR2-sized (27 nm square) block is placed over these areas, it covers some, but not all of the dense area—complete coverage requires a 32-nm square in the top cluster (Fig. 2 A iii) and a 31-nm square in the lower one (Fig. 2 B iii). The size and shape of the blink cluster, combined with the density of labeling makes it likely that these clusters represent tetramers. It is notable that in Fig. 2 A, where the square blink clusters (tetramers) are particularly clear, the blink densities in these squares exceeded 50,000/μm^2. Neither the position of the anti-RyR2 C3-33 epitope nor whether it is a single site associated with the entire tetramer or an individual site on each monomer is known. Given that the fluorophores on the combined primary–secondary antibodies can be as much as 15 nm from the epitope, the images in Fig. 2, A iii and B iii, are consistent with the primary antibodies binding to the upper surface of the tetramer with the secondaries and their attendant fluorophores stationed above the primaries. The difference in size between these clusters and actual tetramers suggests that if multiple tetramers are grouped together, their signals will overlap, as is seen in the upper right in Fig. 2 A iii and the low-center and top of Fig. 2 B iii. Given the constraints of labeling and the randomness of fluorophore blinking, the positions of the tetramers in a cluster cannot be determined precisely, especially when the

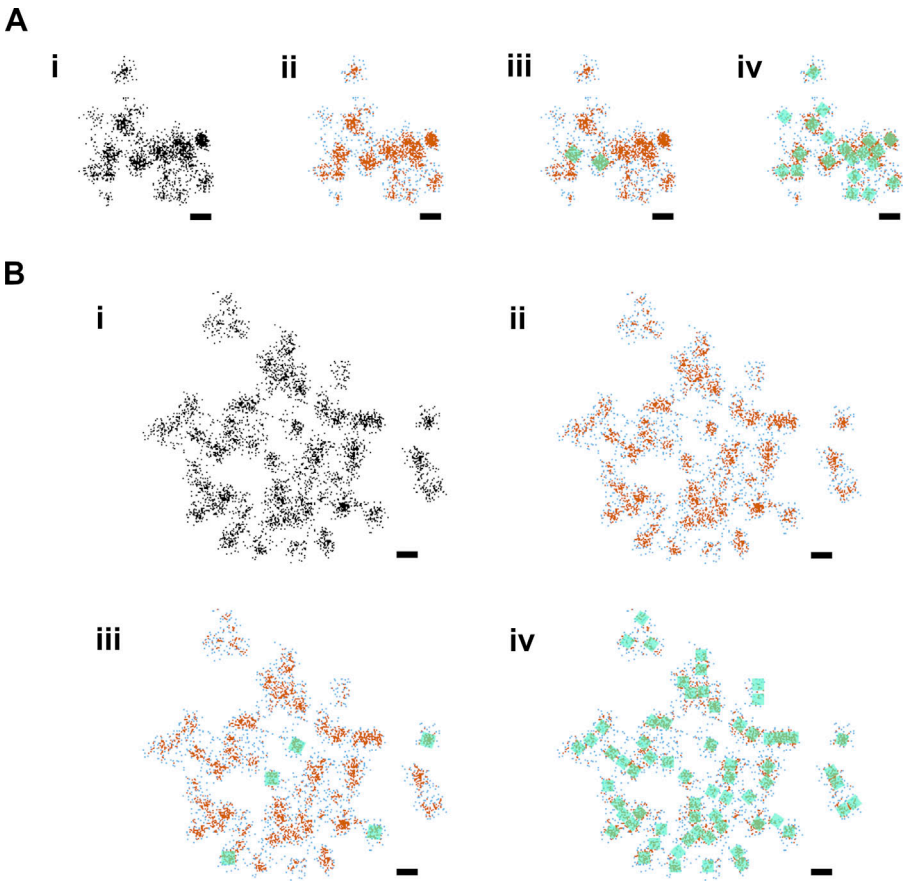

Figure 2. **Tetramer distributions in RyR2 clusters. (A and B)** Analysis of the tetramer distribution of two clusters (A and B) marked in red in Fig. 1 B. **(i–iv)** Descriptions apply to both clusters: (i) blinks before any size filters were applied; (ii) blink density coded so that those blinks above the threshold are in vermillion while those below are in sky blue; (iii) preliminary fit of single tetramers (bluish green); (iv) proposed tetramer distributions. Density threshold was −1.6. Each blink is represented by a 2 × 2 pixel for visibility. Scale bars: 50 nm.

tetramers are grouped together; nonetheless, we can still get a good idea of where they are in relation to each other as well as the number in a cluster. In Fig. 2 B iv, we have labeled 60 tetramers covering 35% of the cluster area; there may be others that have too few blinks to locate. Even with the uncertainty in the orientation and position of some of the tetramers, it is clear that their distribution is neither purely checkerboard nor side-by-side. This can be confirmed by visual inspection of other clusters within Fig. 1 A as well as the surfaces of three other control cells shown in Fig. S4.

We performed the same operation on 10 other clusters where all of the tetramers could be identified. The occupancy (proportion of cluster area covered by the tetramers) ranged from 0.302 to 0.452 with a median of 0.352. This value is lower than that found by tomography, but it is close to the value of 0.33 (Jayasinghe et al., 2018) from a study using DNA-Paint.

Examination of Figs 1, 2, and S4 show that the density and the number of blinks per tetramer varies considerably within and between clusters. In addition, most of the tetramers are surrounded by lower-density blinks that could be incorrectly identified as tetramers. The analyses of Fig. 2 as well as a visual inspection of Fig. 1, A and B; and Fig. S4 show that the arrangement of tetramers in the clusters is heterogeneous. Multiple tetramers clustered together appear frequently as do clusters in which the tetramers appear to be separate. This would fit well with the results of Asghari et al. (2014; 2020), who showed a highly variable tetramer arrangement in control cells.

Phosphorylation effects

Application of 300 nmol/liter ISO for 5 min seems to cause a change in the arrangement and size of the clusters (Figs. 3 and S5). Fig. 3 A has a higher blink density (2,664/μm^2) than the control with the same blink to point ratio of 1.03 and shows both larger clusters and a great degree of crowding. The resolution is slightly improved compared with the control: mean 19.6 nm, range 16.1–24.7 nm. While in some clusters the tetramers are clearly separate and distinct, in others their arrangement appears to be no different from the control cells.

In Fig. 3, B–D, we analyzed three clusters from Fig. 3 A in the same way as in Fig. 2. In Fig. 3, B and C, we applied the same density threshold (−1.6) and then fitted 27 × 27 nm tetramers. The blink density for the clusters was, in order, 25.354, 25.625, and 22.782 per μm^2. As in the controls, the resolution of Fig. 3 A increases to a mean of 20.1 nm, range 18.5–25.1 nm. Fig. 3 D demonstrates that a long, connected string of tetramers can exist in ISO-treated cells. Because it is continuous, the string is almost impossible to fit with realistic tetramer positions and we did not attempt to do so. The ISO-treated surfaces were noisier than the controls and more difficult to fit; nonetheless, we analyzed the tetramer distribution in 10 clusters of the ISO-treated cells. The occupancy ranged from 0.276 to 0.559 with a median of 0.348. Although the median is a little different than that of the control, these values had greater variability with some clusters appearing more separated, giving rise to the low occupancy values.

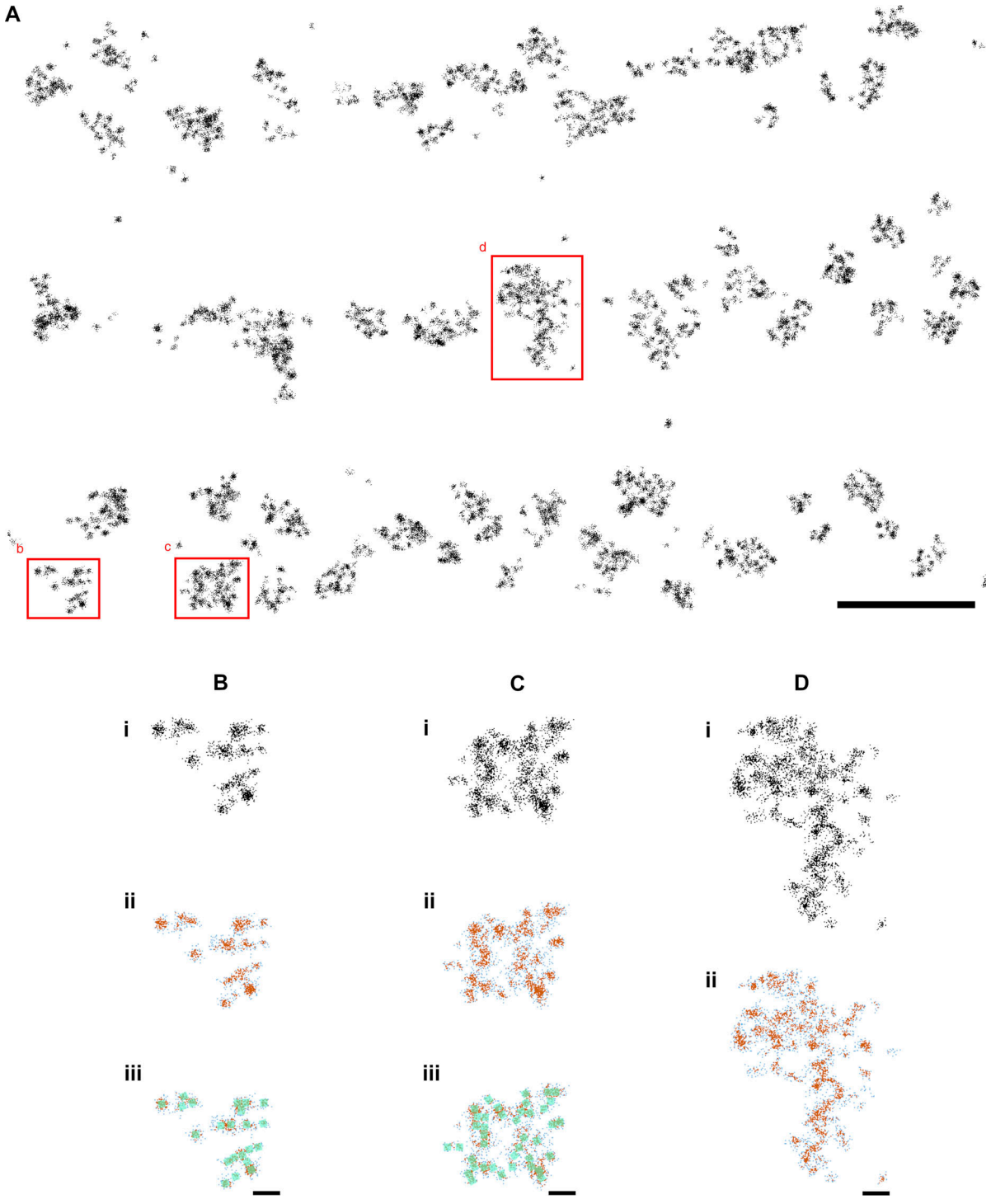

Figure 3. **Blink and tetramer dsitribution in phosphorylated cells. (A)** Blink data showing clusters on the surface of a cardiomyocyte treated with 300 nmol/liter ISO. Area is 12.3 × 4.1 µm. Z lines are parallel to the x axis and 1.7 µm apart. Scale bar: 1 µm. **(B–D)** Three clusters taken from image A. (i) Blinks as they appear in image A; (ii) blink density coded so that those blinks above threshold (−1.6) are in vermillion while those below are in sky blue; (iii) proposed tetramer distributions (bluish green, B and C only). Each blink is represented by a 2 × 2 pixel for visibility. Scale bars: 100 nm.

Clusters and the neighborhood limit

While it may seem visually obvious what a cluster of RyR2 is, the formal definition of what constitutes a cluster is not. As noted in the introduction, a common model for the RyR2 cluster is a tightly packed array, so to belong to a cluster, tetramers would only need to abut one another. Such a model fails when dealing with a group of tetramers as shown in Fig. 2 B, as they look like they are part of one cluster but not all abut or are in contact. Our visual examination of the dSTORM data and our tomographic investigations led us to believe that such an arrangement is a

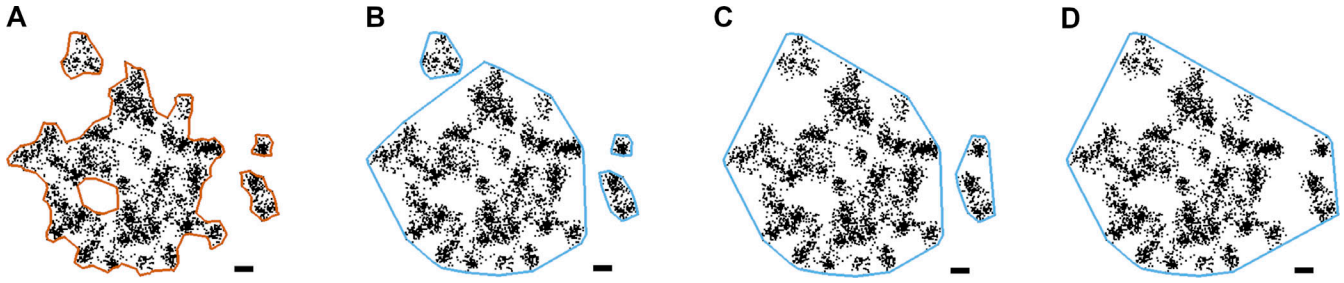

Figure 4. **Neighborhood limit and cluster grouping. (A)** A group of clusters with their α-shape boundaries in vermillion. **(B–D)** Effects of changing the neighborhood limit on the group in A. In each image, the clusters are marked by a convex hull (sky blue). B, 30 nm; C, 50 nm; and D, 80 nm. Increasing the neighborhood limit decreases the number of clusters from four (B) to one (D). Each blink is represented by a 3 × 3 pixel for visibility. Scale bar: 100 nm.

common occurrence and that there had to be a new way of defining what a cluster was and how far apart tetramers could be before they no longer belong to the same cluster. We devised a different criterion for cluster membership: no member of a cluster can be further away from another by more than a specific distance, a metric we called the neighborhood limit (NL). To implement this, we took a two-step approach (see Materials and methods) by first identifying the clusters defined by a 30 nm NL, a value slightly greater than the width of a tetramer (Fig. 4 A and Fig. S3 A). This defined a set of clusters that provided a base for examining clustering with larger NL values. Fig. 4 A shows a group of clusters whose extent is determined by a 30-nm NL and whose boundaries are defined by a fitted α shape (vermillion). In Fig. 4, B–D, clusters that satisfy the particular NL are marked by a convex hull (sky blue). For the 30-nm NL (the base; B), there are four independent clusters. Increasing the NL to 50 nm (C) creates two clusters: one containing the central and top subclusters, while the small cluster on the right is formed from two smaller subclusters. Lastly, the 80-nm limit (D) results in one large cluster with four subclusters. The arrangement in Fig. 3 D also holds for the 100 and 150 nm NL emphasizing that the cluster size does not directly depend on the NL. This figure emphasizes two other properties of the NL—it is both the upper limit of the edge-to-edge distance between two adjacent subclusters in a cluster and the lower limit of the edge-to-edge distance between any two clusters.

Calculating the number of tetramers

Since we are unable to count the number of tetramers in each cluster, we have to translate the cluster area into the number of tetramers; usually, this has been done assuming 900 nm^2 tetramers and an occupancy of 1.0 (Baddeley et al., 2009). Both our occupancy and tetramer size are different: current measurements of the RyR2 turret indicate it is close to 27 × 27 nm (729 nm^2; Van Petegem, 2015), while our results here suggest the occupancy is about 0.35. Because of the subjective and limited nature of these measurements, we decided to use our tomography measurements (Asghari et al., 2020), where the occupancy was found to be 0.5 for controls and 0.53 for cells treated with a phosphorylation cocktail. Given the uncertainties, we thought an occupancy of 0.5 and a tetramer area of 750 nm^2 would provide a reasonable estimate. Combining these values, the number of tetramers is the area divided by 1,500, all values being rounded to the nearest integer. An important and unstated assumption when combining these numbers is that we assume that the occupancy is constant from cluster to cluster. For the same cluster area, our model gives estimates of the number of tetramers that are 60% of those of the Baddeley model. The minimum number of tetramers required to produce a spark is uncertain, as it is a probabilistic event (Iaparov et al., 2021), but 6 is a common number in the literature—with our model, this would translate to 8,250 nm^2 (5.5 rounded up), so areas smaller than this size threshold will be assumed to be unable to generate sparks.

Fig. 5 A i shows a histogram of all of the control cluster area data at a NL of 30 nm (y axis is logarithmic). Excluding the extreme ends, the number of clusters per area decreases exponentially, similar to the findings of Baddeley et al. (2009). The mean and median values are 19.4 × 10^3 and 5.5 × 10^3 nm^2, respectively. Because of the very large number of small clusters, these numbers give a misleading impression of the cluster area distribution. Fig. 5 A ii shows a summed-area plot. In this plot, the areas of the clusters within a range (each bar is 10,000 nm^2 wide) are summed and presented as a percentage of the total cluster area (i.e., summed area of all of the clusters in the control data set satisfying a 30 nm NL). The sum median (51.2 × 10^3 nm^2), which is the midpoint of the summed areas (50% lie below or above) is marked (solid black line) as are the mean (dotted blue line) and the median (solid blue line) from the distribution. Despite numbering in the thousands, clusters smaller than 10,000 nm^2 (seven or fewer tetramers, according to our model) only account for 8% of the total cluster area. If we assume that the tetramer occupancy is a constant, the percent total area is equivalent to the percent total tetramers (the right y axis) and then 92% of the tetramers are in clusters >10,000 nm^2, large enough to generate a spark. 50% of the tetramers are in clusters with areas 20–70 × 10^3 nm^2 while those in areas over 150 × 10^3 nm^2 only account for 3.5% of the total.

The effects of 300 nmol/liter ISO on the clusters (30 nm NL) are seen in Fig. 5, B i and ii. The sum median (59.4 × 10^3 nm^2) as well as the mean (24.5 × 10^3 nm^2) and median (8.08 × 10^3 nm^2) have all increased. The cluster area distribution (Fig. 5 B i) has fewer small clusters; the initial exponential decrease is noticeably less steep than the control after which it reverts to a similar rate of decline. The summed cluster area graph (Fig. 5 B ii) shows a shift to the right—only 6% of the tetramers are in

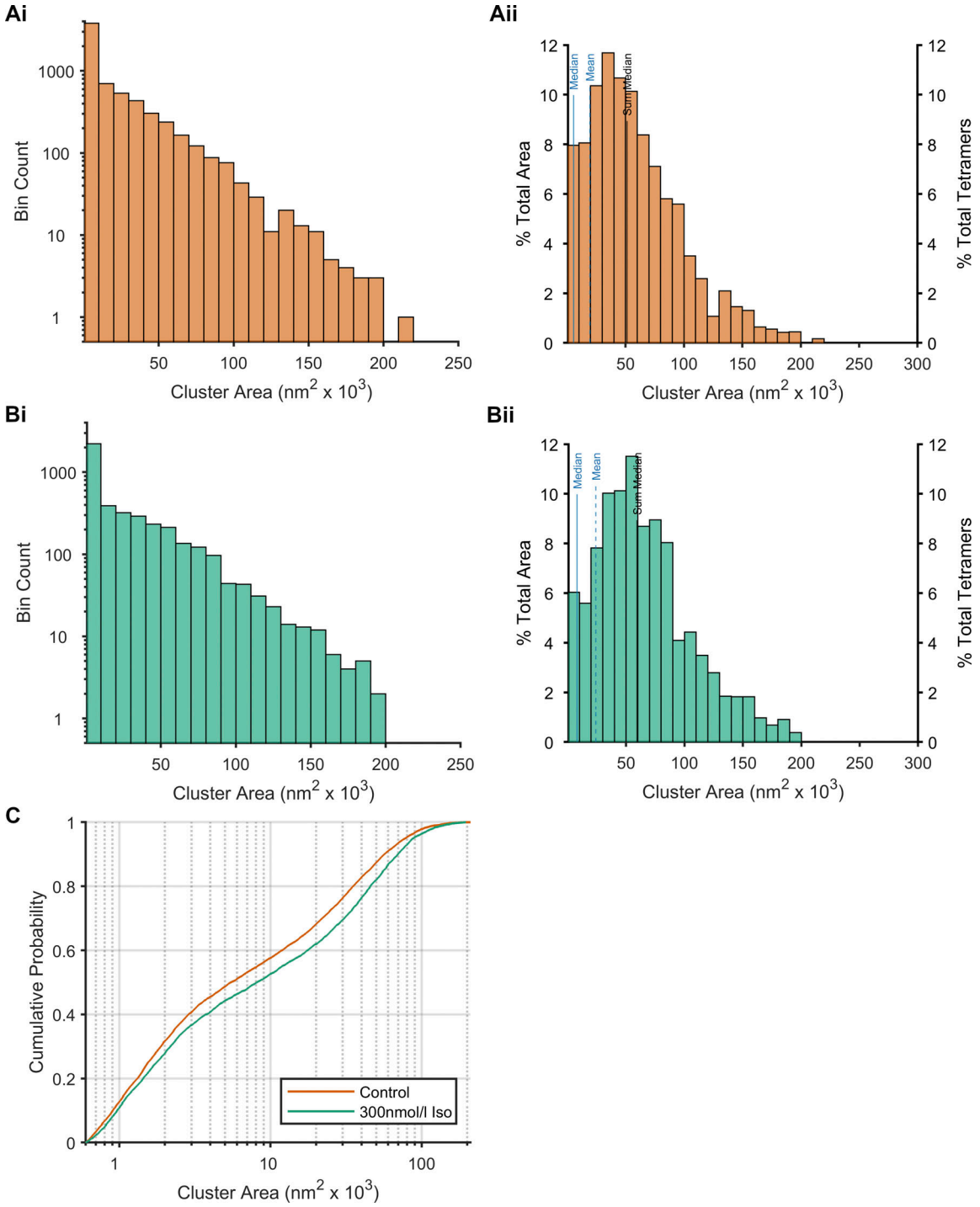

Figure 5. **Cluster area distributions. (A)** Control cells: (i) Cluster area distribution. Each bar is 10^4 nm^2 wide and the y axis is logarithmic. (ii) Total area contribution from the summed areas of the clusters defined by each bar. **(B)** Cells treated with 300 nmol/liter ISO. (i) Cluster area distribution; bar size and y axis is the same as control. Compared with control cells (A i), the distribution is flatter for the lower value areas. (ii) Total area contributions. Changes in B i are reflected in a reduction in the contribution from small areas and a shift in the sum median to the right. **(C)** CDF of the cluster areas of control and ISO-treated myocytes. The distribution of the ISO-treated cells is significantly shifted to the right ($p < 10^{-6}$).

clusters <10,000 nm^2 while 13% are in clusters <20,000 nm^2 compared with 16% of the control. The 20–70 × 10^3 nm^2 group has slightly fewer tetramers (48% versus 50%) and the gains are in the 70,000 nm^2 region, with 4.5% in clusters over 150 × 10^3 nm^2.

A statistical comparison of the distributions in Fig. 5, A i and B i, showed that the ISO cluster area distribution is significantly shifted to the right of the control, $P < 2 \times 10^{-12}$. For clarity, we display the distributions using a CDF so that the difference in the groups can be clearly seen (Fig. 5 C). The scale is logarithmic and

Table 1. **Cluster area metrics**

NL (nm)	Cluster numbers		Area (× 10^3 nm^2)						Probability
	Con	ISO	Control			ISO			ISO = Control
			Median	Mean	Sum median	Median	Mean	Sum median	
30	6,615	4,228	5.5	19.4	51.2	8.1	24.1	59.4	2×10^{-12}
40	5,883	3,799	7.7	21.8	53.6	11.3	26.9	61.6	3×10^{-12}
50	5,486	3,584	9.6	23.4	55.0	14.3	28.9	63.9	9×10^{-13}
60	5,220	3,321	11.1	24.6	56.5	16.7	30.7	66.0	3×10^{-14}
80	4,796	2,998	13.2	26.8	59.7	19.7	34.1	71.4	2×10^{-15}
100	4,457	2,732	15.3	28.8	63.7	23.5	37.4	76.7	9×10^{-16}
150	3,670	2,122	19.4	34.8	75.3	28.6	47.9	97.8	5×10^{-13}

NL = neighborhood limit. Con = control. ISO = 300 nm/liter ISO.

indicates an increase of up to 40% in the ISO-treated cluster areas. Since the cluster sizes for NLs over 30 nm are a combination of the 30 nm values, we would expect that CDFs for these values would also be significantly different (Table 1).

Fig. 6 shows the effect of the NL values of 40, 60, 100, and 150 nm on the summed areas for both cell types. In both controls (Fig. 6 A) and the ISO-treated cells (Fig. 6 B), the darker regions of the bar represent the proportion of the area (or tetramers) that are in clusters with multiple subclusters (multiclusters; we use the term single clusters for those that are unmatched). Increasing the NL increases the proportion of clusters that are multiclusters and reduces the mid-range cluster areas (30–70 × 10^3 nm^2) while increasing the number with larger cluster areas. As shown above, the ISO cluster areas are significantly larger than the controls for all NL, a difference which is reflected in the summed areas. The remarkable increase in the size of the ISO 150 nm clusters necessitated a 66% increase in the length of the x axis while keeping the same scale, indicating that other properties of the clusters, like the nearest neighbor distance, are significantly different in ISO cells from those of the controls.

For all NL values, there are always a small number of clusters, including multiclusters <10,000 nm^2 in area. These clusters constitute a small proportion of the total, which decreases with increasing NL. Independent of the NL, the cluster areas cover a wide range of values, showing that there is no direct link between the two. Even though increasing the NL produces larger clusters, a significant number of mid-range and smaller clusters always remain.

The number of tetramers required to generate a spark depends on the arrangement and density of the tetramers, so a single number cannot describe the likelihood of spark generation. In Table 2, we show the percentage of tetramers in clusters larger than two thresholds—6 tetramers (cluster area >8,250 nm^2) and 20 tetramers (cluster area >29,250 nm^2). Depending on the NL, between 93 and 97% of the tetramers in control cells are in clusters sized 6 tetramers or more, while between 74 and 86% are in clusters 20 tetramers or more. The ISO-treated cells increase those values by about 1% for the 6-tetramer minimum and 5% for clusters containing 20 tetramers or more.

Multicluster characteristics

Table 3 shows the percentage of multiclusters that have two or more subclusters for both cell treatments and all of the NL. The 5+ column represents the sum of multicluster percentages for all groups from five to maximum for that NL. Clusters with two subclusters predominate for all control NL and all ISO, except for the 150-nm NL. For the low subcluster numbers, the control and ISO parallel each other, with the ISO having slightly fewer clusters, with two subclusters and slightly more with three subclusters. The greater deviations occur for the 80–150 nm NLs where ISO has many more clusters in the 4–5+ subcluster range. An important insight into the arrangement of the clusters can be had from the percentage total clusters column. Only 10.3% of control clusters are separated by 30–40 nm while 15.7% are separated by 30–50 nm, so 5.4% are separated by 40–50 nm. There is little difference between control and iso values. The 29.6% estimate for 100 nm is much lower than that found by Baddeley et al. (2009), who reported that 50% of the clusters were within that distance. That only 40% of the clusters were within 150 nm may seem low, but this is associated with about 70% of the area. About 30% of the balance (single clusters) are smaller than the size threshold of 8,250 nm^2. The wide subcluster distribution for the control cells at the 150 nm NL is in contrast with that reported in a study of interior clusters (Macquaide et al., 2015), which found a tight distribution centered on three subclusters per cluster. For comparison with other published data, the mean number of subclusters in control cells is 2.62 at 100 nm NL and 3.00 at 150 nm NL. Kolstad et al. (2018) reported 2.8 at 100 nm and 3.7 at 150 nm NLs, while the larger interior clusters are reported to have 3.41 subclusters at 100 nm (Hou et al., 2015). The effect of ISO was to cause a significant increase in the mean number of subclusters to 2.81 at 100 nm NL ($P = 0.0001$) and 3.41 at 150 nm NL ($P = 8 \times 10^{-6}$).

Examining the 150 nm NL, we found no relationship between the number of subclusters and the area of the clusters for either the control or the ISO-treated cells (Fig. 7 A), although there is a slight upward trend at the higher subcluster values. In this graph, the control points (vermillion) and the ISO (bluish-green) are slightly offset from their integer subcluster values so that they can both be seen. In some places, there are so many points

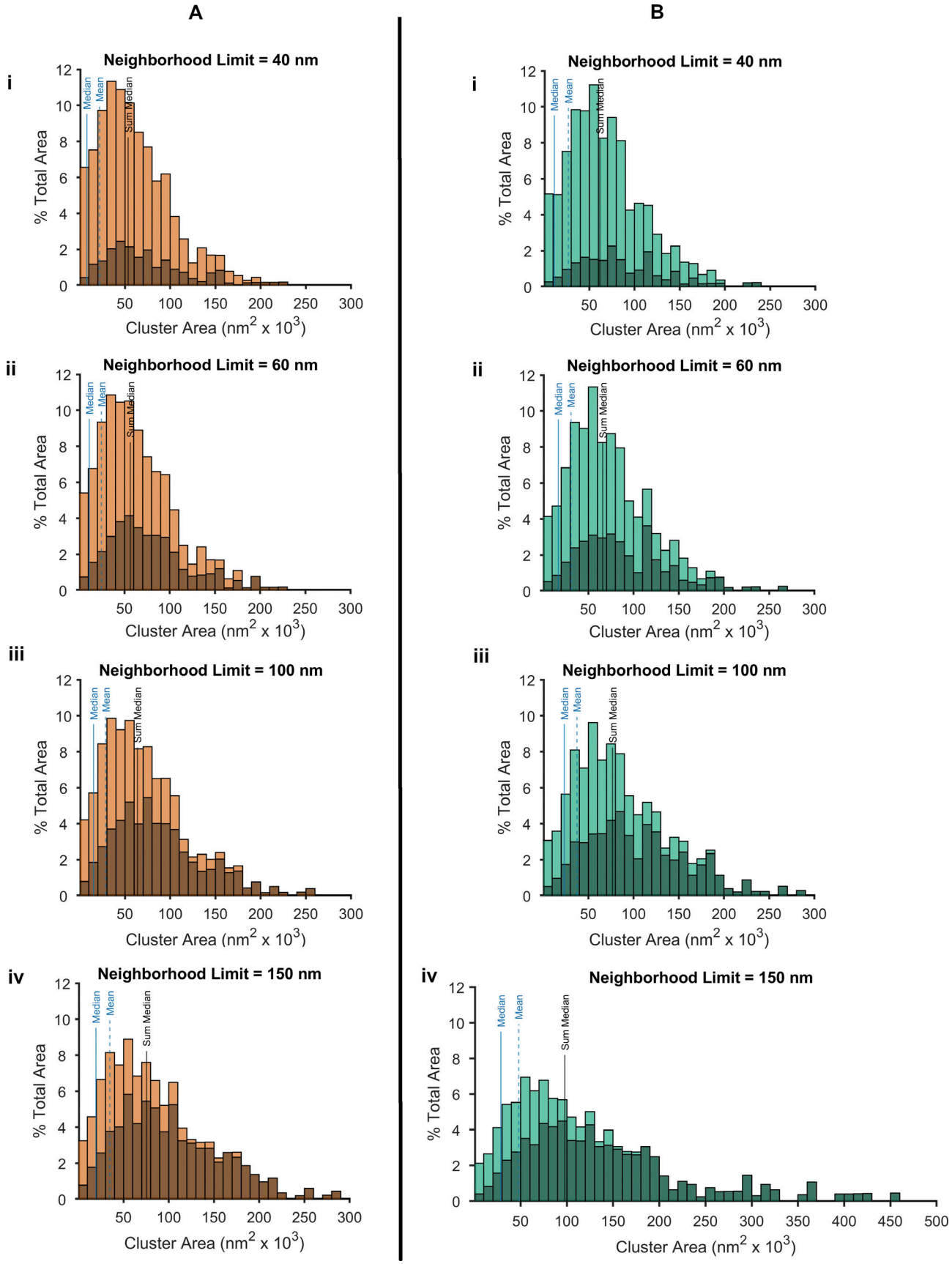

Figure 6. **Summed area distributions and the neighborhood limit.** Summed area distributions for (A) control cells and (B) cells treated with ISO. (i–iv) For both A and B, the NLs are: (i) 40 nm; (ii) 60 nm; (iii) 100 nm; and (iv) 150 nm. The dark areas represent the proportion of the areas that are due to multiclusters. All axes are to the same scale including B iv, where the x axis was expanded 60%. The values of mean, median, and median sum are listed in Table 1.

Table 2. **Percentage tetramers in clusters above a given size**

NL (nm)	% Tetramers in clusters containing			
	≥6 tetramers		≥20 tetramers	
	Control	ISO	Control	ISO
30	93.2	94.9	74.4	81.2
40	94.4	95.7	77.0	82.9
50	95.0	96.3	78.4	84.0
60	95.5	96.6	79.4	85.0
80	96.1	97.1	81.2	86.8
100	96.5	97.6	82.6	88.2
150	97.3	98.3	86.2	91.5

NL = neighborhood limit. ISO = 300 nm/liter ISO.

that they appear as lines. From the graph, it can be determined that the clusters in Fig. 6 B iv that are >300 × 10^3 nm^2 have between 4 and 16 subclusters, that the cluster with the most subclusters (18) is not the largest, and that both control and ISO in the 200–300 × 10^3 nm^2 range can have any value from 2 to 11 subclusters.

We also examined the relationship between the largest subcluster and the second largest for the 150-nm NL for both the control and ISO cells (Fig. 7 B). The two interior black lines in each graph represent the threshold size (8,250 nm^2, equivalent to six tetramers) below which sparks are unlikely to be generated. The edge in the scatter plot is the line of equality since each second largest must be smaller or equal to the largest. Clearly, there is no relationship between the two subclusters, but the mass of points near the x axis made us wonder how many multiclusters had a second-largest cluster too small to generate a spark (if there is a third- or fourth-largest, it must be true of them too). There are also a number of clusters that lie within the box created by the threshold lines—these are multiclusters in which all their component clusters are below the threshold size and unlikely to generate sparks. Table 4 identifies these clusters for NL and both cell treatments.

Table 4 has two parts: the first lists the percentage of multiclusters with their largest subcluster above the threshold size. Depending on the treatment and the NL, 10–20% of the multiclusters have all their subclusters below the threshold corresponding to 0.7–2.9% of the area covered by the multiclusters—these are the clusters within the box (Fig. 7, B i and ii). The second part of Table 4 lists those clusters that have the largest cluster above the threshold size but the second largest below it. There are a surprisingly large number of clusters that fall in this category constituting 48.7–65.1% of the multiclusters and between 39.4 and 70.1% of the total area covered by them. The distribution (i.e., how many of the clusters have two, three, or more subclusters) of these subclusters parallels those seen in Table 3. For the 40-nm NL, 86% have two and 11% have three subclusters, while at the 150-nm NL 65% have two, 20% have three, 10% have four, and 3% have five subclusters (figures are averages of the control and ISO values which track each other closely). This distribution and the median area (~29 tetramers) suggest that most of these clusters consist of one midsize cluster matched with one or more small (<6 tetramers) clusters. No matter how many subclusters there are, they all are below the threshold for producing a Ca^{2+} spark, and when ordered by size, each one is the same or smaller than the next. It is likely that most of these multiclusters, especially those at higher NLs, will act as if they are singleton clusters for spark generation.

Other cluster parameters and the effects of ISO

Table 5 shows two other parameters that describe the clusters: edge-to-edge distances and the dimensions of the fitted ellipses. The edge-to-edge differences increase steadily with the NL, almost doubling in value between 30 and 150 nm NLs. The 100 and 150 nm values 225.3 and 265.9 nm are greater than those reported by Kolstad et al. (2018), 215 and 203 nm, respectively. After phosphorylation, the clusters are significantly closer together than the controls for all NLs (Fig. 8 A).

The median eccentricity of the ellipses surrounding the clusters was ~0.54 giving a major to minor axis ratio of about 1.4. This value is much smaller than the aspect ratio of 1.9 reported by Baddeley et al. (2009), suggesting that the clusters they studied were thinner or longer than ours, but the difference could also arise from the different methodologies that we used. In all of the data examined, very few clusters were symmetrical (ratio ≈ 1) or very elongated (ratio > 3). There was

Table 3. **Multiclusters and their subcluster characteristics**

NL (nm)	Subclusters per NL				% Multiclusters with this many subclusters								% Total clusters		% Total area	
	Median		Max		2		3		4		5+					
	Con	ISO	Con	ISO	Con	ISO	Con	ISO	Con	ISO	Con	ISO	Con	ISO	Con	ISO
40	2	2	7	5	85.2	85.1	11.9	11.8	2.3	2.8	0.6	0.3	10.3	9.6	20.0	18.6
50	2	2	8	5	78.9	77.3	16.2	18.3	3.3	3.3	1.6	1.1	15.7	15.3	30.3	27.8
60	2	2	8	6	76.2	71.3	16.9	21.0	4.4	4.6	2.7	3.1	19.5	19.5	37.0	34.7
80	2	2	9	10	68.5	64.5	20.6	21.1	7.0	8.9	3.9	5.6	25.0	25.9	46.7	45.7
100	2	2	11	12	63.5	56.3	22.3	22.9	8.7	11.0	5.5	9.7	29.6	30.3	54.5	53.4
150	2	3	12	18	52.2	45.5	23.9	21.5	11.6	12.8	12.3	20.1	39.6	40.7	68.8	71.9

NL = neighborhood limit. Con = control. ISO = 300 nm/liter ISO.

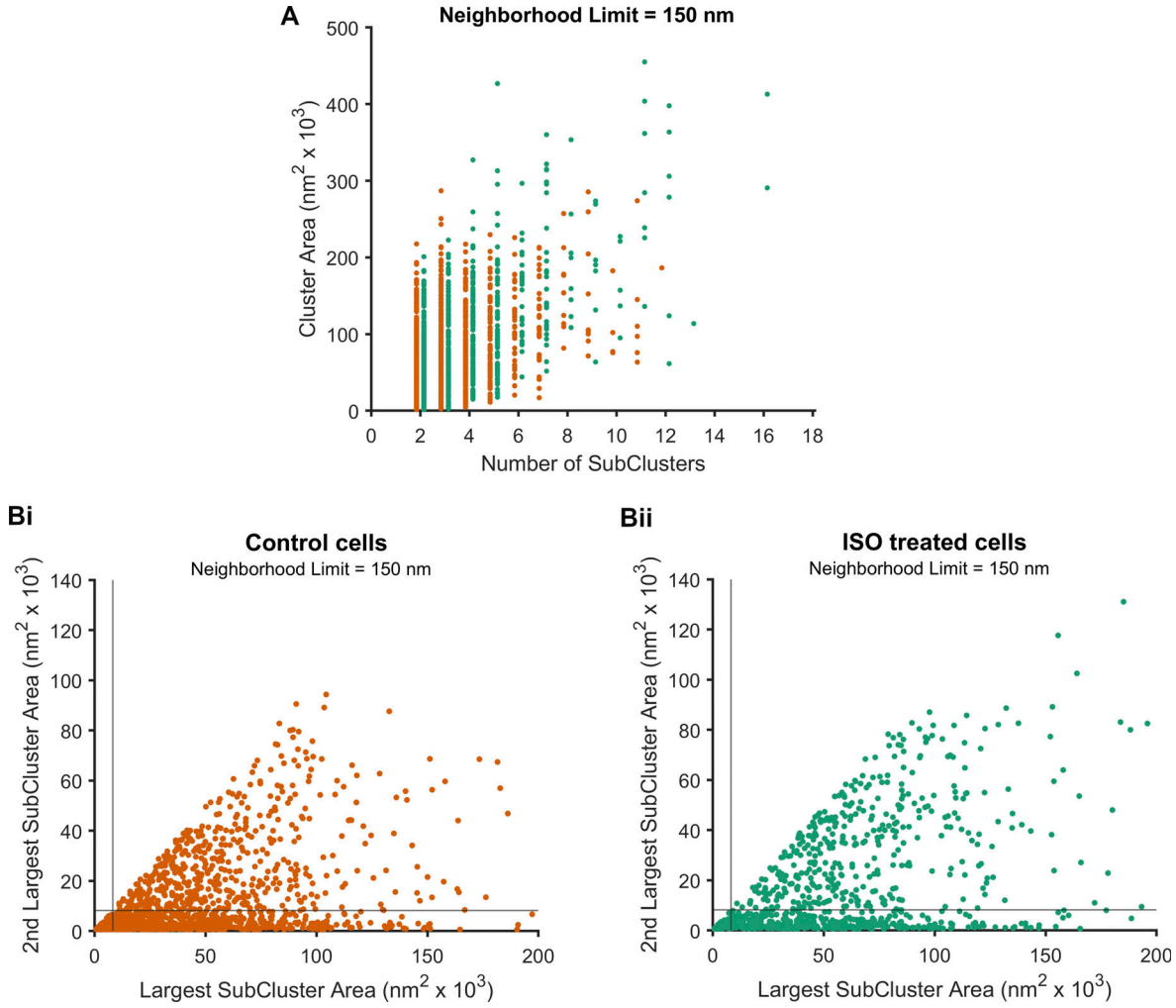

Figure 7. **Subcluster distributions at a 150 nm NL. (A)** Plot of the number of subclusters versus cluster area. Control cell values (vermillion) are offset from ISO values (bluish-green). **(B i and ii)** Plot of largest subcluster versus second largest subcluster (i) control cells (ii) ISO-treated cells.

Table 4. **Multiclusters–subcluster thresholds**

NL(nm)	Largest subcluster above threshold						Second largest subcluster below threshold					
	% Total multiclusters		%Total multicluster area		Median area (× 10³ nm²)		% Total multiclusters		% Total multicluster area		Median area (× 10³ nm²)	
	Con	ISO	Con	ISO	Con	ISO	Con	ISO	Con	ISO	Con	ISO
40	80.7	84.0	97.1	98.4	41.8	52.1	65.1	68.3	70.1	71.3	36.8	47.2
50	80.8	84.5	97.3	98.4	45.6	51.9	64.0	66.9	70.1	68.2	40.6	45.7
60	80.9	84.6	97.4	98.4	48.0	53.9	62.5	64.4	67.7	63.7	42.4	45.8
80	81.9	86.6	97.7	98.8	50.0	58.6	59.2	59.0	60.1	53.0	41.6	46.2
100	82.9	88.4	97.9	99.0	52.5	63.2	56.5	54.7	54.4	44.9	42.2	45.3
150	84.2	90.6	98.4	99.3	57.9	75.7	48.7	44.4	39.4	29.1	40.6	46.3

NL = neighborhood limit. Con = control. ISO = 300 nm/liter ISO.

no relationship between the ellipse axis ratio and the area of the cluster. Phosphorylation increases both the major and minor axes of the ellipse (Fig. 8 B and Table 5), indicating an expansion of the clusters on phosphorylation; examination of the ellipse eccentricity shows a slight increase, but it is doubtful that this has any meaning.

Table 5. **Edge-to-edge distance and ellipse parameters**

NL (nm)	Edge-to-edge distance (nm)			Minimum ellipse						Probability
				Major axis (nm)		Minor axis (nm)		Eccentricity		ISO = control
	Con	ISO	Probability ISO = control	Con	ISO	Con		ISO	Con	ISO
30	137.6	127.3	0.036	100.7	114.2	66.0	74.3	0.53	0.54	3.4×10^{-12}
40	162.2	146.1	6.2×10^{-9}	110.5	124.3	72.9	80.5	0.53	0.54	1.8×10^{-11}
50	177.9	159.6	5.7×10^{-13}	117.4	132.4	75.8	85.2	0.53	0.54	2.7×10^{-11}
60	189.2	171.7	7.4×10^{-12}	122.9	139.7	78.8	89.6	0.54	0.54	4.4×10^{-13}
80	209.4	190.6	2.6×10^{-14}	133.1	153.9	84.1	96.6	0.54	0.54	4.4×10^{-13}
100	225.3	208.2	5.1×10^{-12}	143.1	167.7	89.1	103.8	0.55	0.55	7.4×10^{-13}
150	265.9	255.3	6.6×10^{-6}	175.5	213.2	103.9	123.9	0.57	0.57	1.6×10^{-9}

All values are means. NL = neighborhood limit. Con = control. ISO = 300 nm/liter ISO. Ellipse probability is the maximum of the probabilities for the major and minor axes control versus ISO comparisons.

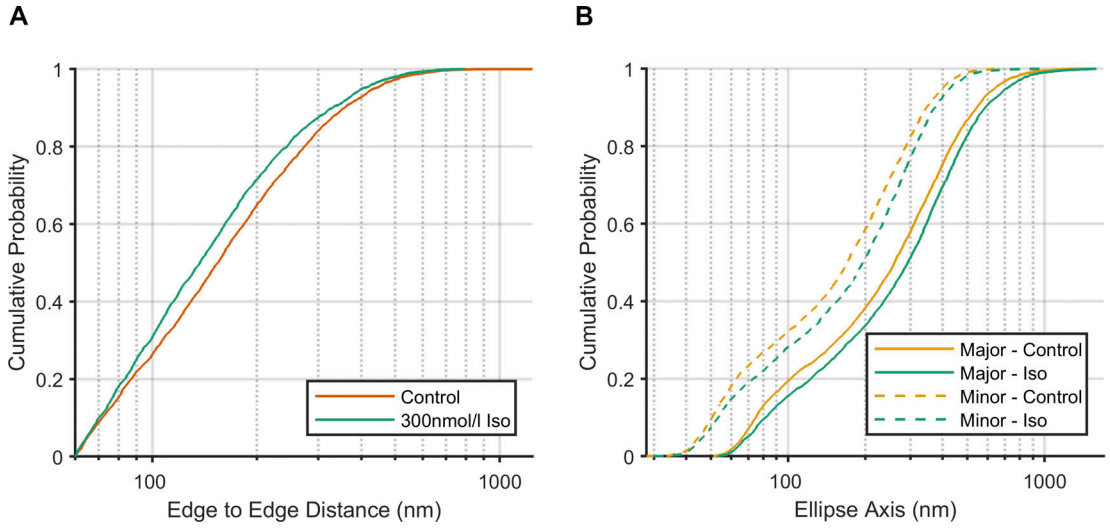

Figure 8. **Effect of ISO on cluster edge-to-edge distances and ellipse axes. (A)** CDF of cluster edge-to-edge distance (NL = 60 nm) showing the ISO curve is significantly shifted to the left indicating a general decrease in the distance. **(B)** CDF of the major and minor axes of the minimum ellipse fitted to each cluster (NL = 60 nm) showing that the length of both axes is significantly increased by ISO. The mean values and significance for both parameters at other values of the NL are listed in Table 5.

Surface coverage

We also measured the changes in surface coverage due to the ISO treatment. For each image, we calculated the ratio between the sum of all the cluster areas in an image and the area imaged. The data passed a normality test so we report both mean and standard error. The area covered by control cells was 6.31 ± 0.30%, while ISO-treated cells had a coverage of 8.00 ± 0.31%; a *t*-test showed that this difference was significant (P = 0.00034).

Assuming a constant occupancy, the overall tetramer density was 42.04 ± 2.02/μm² for the controls and 53.33 ± 2.09/μm² for the ISO-treated cells; as these numbers are derived from the coverage, they are also significantly different. The control tetramer density allows us to estimate the total number of RyR2 on the surface of the ventricular myocyte. If we assume that the myocyte is represented by a cylinder 20 μm in diameter and 120 μm in length, it has a volume of ∼37.6 pl (Scriven et al., 2002) and a surface area of 7,540 μm², which in turn translates to ∼317,000 tetramers, about 10% of the total that was previously estimated (Bers, 2001).

We calculated the cluster density (number per μm²) only for the 30-nm NL. The cluster density increased significantly on ISO treatment; controls 2.98 ± 0.11/μm²; ISO 3.41 ± 0.14/μm² (P = 0.016). Both these numbers are less than that previously reported for control cells 4.5 ± 0.3/μm² (Kolstad et al., 2018).

Evaluating the relationship between blinks and tetramers

Shen et al. (2019) proposed a linear relationship between the number of blinks and the number of RyR2 based on their observations of the cell surface; they then used this approach to estimate the number of receptors inside the cell where direct

visualization of the receptors is considerably more difficult because of the angles at which the receptors are present and because the Z resolution is much lower than that in the XY plane. Since our experiments used a similar methodology, we investigated our data to see if we could determine a similar relationship.

If the number of RyR2 is directly proportional to the area (Jayasinghe et al., 2018) and the relationship is linear, we would expect the ratio of blinks-per-cluster to cluster area to be narrowly grouped about a constant value. For this analysis, we examined two data sets, one from a group of four controls and the other from a group of four ISO-treated cells; each set was collected in a single session with fixed system settings, although the ISO-treated set had a higher laser intensity. We measured the number of blinks in each cluster and divided that by the area of the cluster. We used the data defined by the 30-nm NL, noting that since the higher NL clusters are built from these base clusters, the results would only differ in scale. Plots from both data sets (Fig. 9, A i and B i) show a single peak with a broad distribution, different from the narrow distribution expected from a simple linear relationship. If there are a significant number of points in a cluster where there are multiple blinks, this might explain the distribution. In the control, cells between 3 and 4% of the blinks are multiple and in ISO-treated cells, 3–7%. To correct for this, we only counted those points where the blinks occurred rather than the blinks themselves, in effect removing any blink multiple. This produced plots (Fig. 9, A ii and B ii) with a distribution as broad as those of Fig. 9, A i and B i, indicating that the multiple blinks were not responsible.

The "single blink" data set allowed us to analyze the relationship between blinks and cluster area. This produces a point cloud that can be fitted by a linear relationship (lines in Fig. 9, A iii and B iii), a plot similar to that of Fig. 2 B of Shen et al. (2019). The inset shows a magnified view of the origin and reveals that the relationship breaks down for small values (blinks per cluster <100) where numerous point values result in the same area value. The initial cone shape of the point cloud and its wide dispersion about the fitted line suggest that the data is heteroscedastic. Applying the Breush–Pagan test confirms that it is strongly so (values: A iii = 322; B iii = 429; $P < 10^{-15}$ for both) violating the condition for a valid linear regression. A heteroscedastic, cone-shaped data set is often associated with a variance that increases with an increasing x value so that the estimates for the y value have a steadily increasing error giving rise to the cone. This is not the case here because the area measurements (not estimates) have a low variance independent of the size of the cluster (see Materials and methods). The point cloud is real and not due to errors of measurement. Given a point P on the x axis, the actual area could correspond to anywhere on the vertical line from P that intersects the point cloud so that, at best, the equation is only weakly predictive.

Discussion

Our identification of tetramers in Figs. 2 and 3 may be questioned because the FRC-derived resolution had values equal to or slightly less than the size of the tetramer. In Fig. 2, we found isolated groups of blinks, each in the form of a square (Fig. 2, A iii and B iii). Our use of an anti-RyR2 antibody, the high-blink density in the groups, and their shape and size (31–32 nm) led us to identify these blocks as tetramers. We also found that a high-blink density better defined the tetramer shape and that the resolution increased when low-density blinks were omitted. The presence of well-defined tetramer-like objects suggests that the local resolution is much higher (a lower value) than the FRC-derived image-wide values. We conclude that the majority of the multiple high-density regions which can be seen in Figs. 1, 2, 3, S4, and S5 represent tetramers. In both of the Fig. 2 clusters, there are groups of connected densities, with one dimension the approximate width of a tetramer, making it likely that these are signals from adjacent tetramers. If the local resolution was as low as the FRC implies, we would expect the cluster group to be more diffuse and much wider than a single tetramer, which is not the case.

The density threshold, used in Figs. 2 and 3, is an imaging tool that enhances the contrast between areas of high- and low-blink density; it does not alter the data and acts as a guide when the borders of the high-density regions are unclear. As such, our identification of the blocks as tetramers does not depend on a precise value for the threshold.

Given the uncertainties, our placement of the tetramers in Figs. 2 and 3 is a subjective process, representing our best guess, and as such, we are limited in the conclusions that we can reach about the numbers, positions, and orientation of the receptors. Nonetheless, we have shown that the distribution of RyR2 receptors in situ is not a packed, checkerboard, or distributed array, and that the architecture is most like those observed by our group using electron tomography (Asghari et al., 2014, 2020). Further, the tetramer occupancy is of the order of 50% or lower. It is unlikely that either of these observations is an artifact as they come from different techniques with separate measurements from either the cell surface or its interior. In particular, the method of fixation we used (2% paraformaldehyde) was much milder than the techniques used in electron microscopy and tomography and caused little or no shrinkage.

Our results for the control cells differ from those of previous authors. In a number of studies, these differences, wholly or in part, are due to a lower resolution as well as the assumption that the tetramers are organized in a fixed, ordered array. In addition, we used a milder fixation protocol and higher values of laser excitation resulting in greater detail in our images. We found that in order to see well-defined tetramers (as in Fig. 1), we needed a blinking rate of at least 800/μm^2 in addition to our higher resolution. Although clusters on the interior are known to be larger than those on the surface, they seem to differ in scale (Hou et al., 2015) rather than structure. This, in addition to the similarities in tetramer arrangement, gave us the confidence to use data from interior measurements to guide our interpretation of the surface data in this paper.

A study using DNA-Paint to image the cardiomyocyte (Jayasinghe et al., 2018) found that the nearest neighbor distances between the tetramers were a single-mode distribution with a median of 40 nm. Most tetramers they see are isolated—very few are close enough to physically interact.

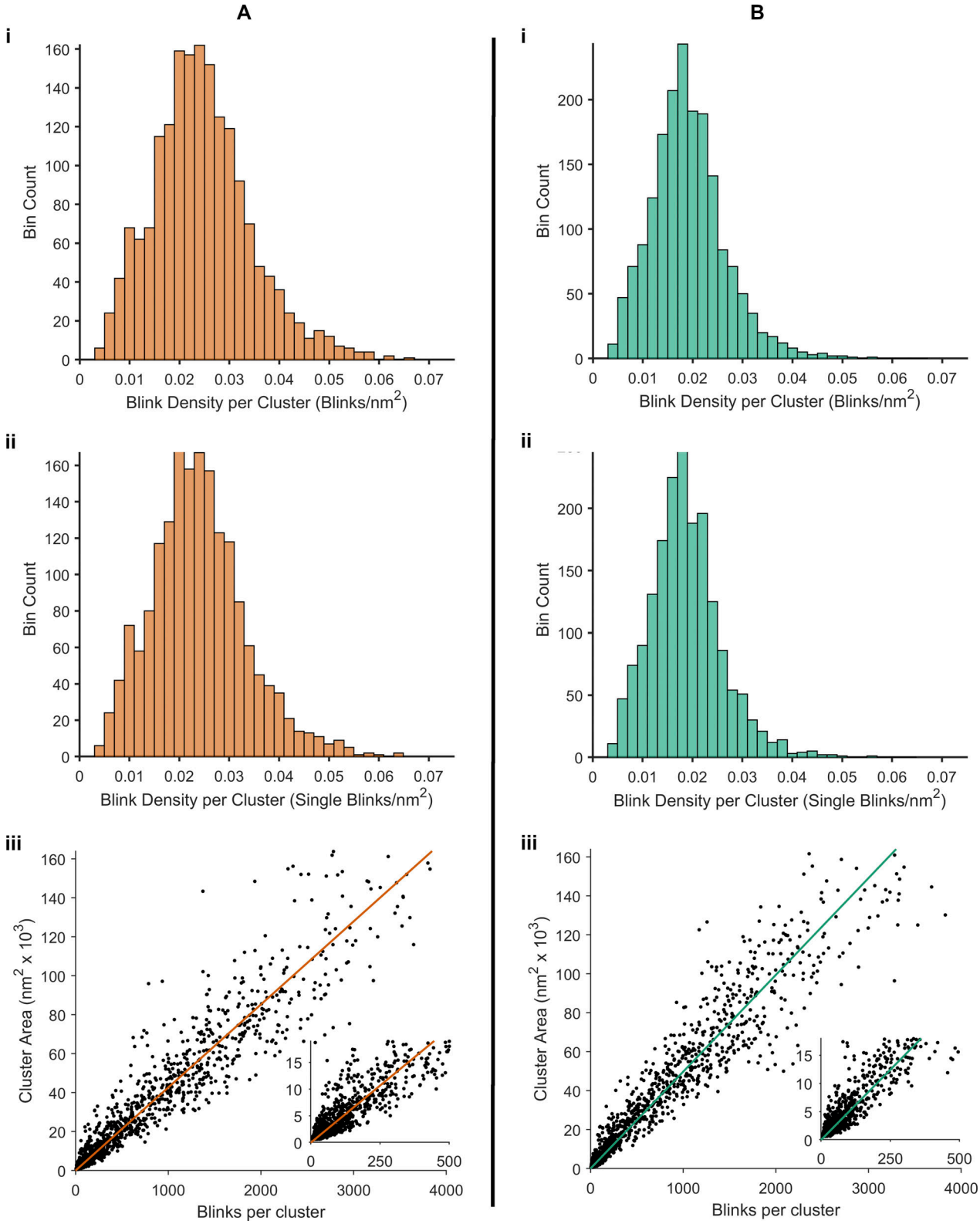

Figure 9. **Measuring the relationship between the cluster area and the number of blinks per cluster. (A i–iii)** Control cells: (i) histogram of the blink density per cluster, (ii) histogram of the single blink density per cluster, (iii) scatter plot of cluster area versus blinks per cluster (BPC). Inset is a magnification of the first 500 points. Equation of the line is 42.64 BPC (passes through 0,0). **(B i–iii)** The same in ISO-treated cells. In ii, the equation of the line is 49.73 BPC.

While this result is very different from our observations, we cannot explain this disparity, although their experiment differed in that they increased the external $[Ca^{2+}]$ to 200 µmol/liter compared with our 1 mmol/liter and used laminin instead of poly-L-lysine to attach their myocytes to the coverslip. Whether these changes are sufficient to explain the differences is unclear.

Since the tetramers in a single cluster are not in a contiguous array, we used the NL to define clusters in which the tetramers did not always abut. The two-step approach we used reflects the dual nature of the NL: at 30 nm it determines the structure of single clusters; at values >30 nm it determines if, and how, those clusters are grouped, setting the maximum edge-to-edge distance between subclusters within a cluster, while also setting the minimum distance between clusters. Using the two-step approach gave us information on the individual subclusters and allowed us to do a detailed analysis of multiclusters.

While the effect of increasing the NL is to increase the number of multiclusters, producing more large clusters and reducing their overall number (Fig. 6 and Table 1), it does not determine the extent of the clusters. The 30-nm NL can produce single clusters that stretch many hundreds of nanometers, while the 150-nm NL has numerous single and multiclusters that are small or medium sized (Fig. 6 A iv). A secondary effect of the NL can be seen on examination of the control images (Fig. 6, A i–iv). The proportion of tetramers in the 20–100 × 10^3 nm^2 (13–67 tetramers) range is diminished as the NL is increased, indicating that much of the multicluster formation comes from at least one cluster in that range. The response to ISO is similar although the histogram is shifted to the right so that there are fewer small clusters. Increasing the NL produces more large clusters than the control, until 150 nm, where there is an explosive growth that produces clusters ranging in size from 250 to 455 × 10^3 nm^2 (167–303 tetramers), reflecting both the larger size and the reduced edge-to-edge distance of the ISO clusters.

As is shown in Fig. 5 A ii and Table 2, the majority of tetramers are in clusters large enough to produce a spark even when we assume there is no interaction between the clusters (30 nm NL) since 93.2% are in clusters greater than or equal to 6 tetramers and 74.4% are in clusters ≥20 tetramers. These numbers increase with both ISO treatment and the NL. Although these numbers do not preclude it, no assumption of Ca^{2+} diffusion between clusters is necessary to have a fully functional cell. A model of the excitability of tetramer clusters based on our earlier work has been investigated by the Zahradnikova group (Iaparov et al., 2021) where, assuming all tetramers had the same excitability, they found that the probability of spark generation depended on three factors: the number of tetramers per cluster, their density, and the distance between clusters. The area of effect of every cluster depends both on its properties and those of its neighbors and it is unlikely a single value like the NL could account for such complexity.

Superclusters and the CRU

Baddeley et al. (2009) noted that some clusters were close enough to each other to act as a functional group or CRU. They named these groups "superclusters," which they defined as those clusters within a 100-nm (Sobie et al., 2006) edge-to-edge distance from each other. Doing so increased the mean tetramer per cluster from 13.6 to 21.9. With a 100-nm NL, the area of both single and multiclusters in our data ranges from 10 to 170 × 10^3 nm^2 (6–113 tetramers), and superclusters constitute 29.6% of the clusters and cover 54% of the area (Table 3). Nearly 57% of the multiclusters constituting ∼55% of the multicluster area are functionally (from the perspective of spark generation) single clusters (Table 4), and so many of the superclusters behave in a way that is no different from their unmatched counterparts. If functional coupling is a discriminating criterion for a multicluster to be classified as a supercluster, most of those with below-threshold partners should be excluded. Identifying the CRU with superclusters alone is problematic when there are so many single clusters, both structurally and functionally.

A CRU is a term that was synonymous with a structural dyad, but for superresolution studies, it has been co-opted to mean those clusters defined by a 100 or 150 nm edge-to-edge distance (Baddeley et al., 2009; Macquaide et al., 2015; Kolstad et al., 2018). Superresolution imaging cannot, at this time, detect the edges of the dyads, so it is quite possible that there are multiple boundaries within a single 100 or 150 nm NL multicluster, a view supported by Hayashi's tomographic data (Hayashi et al., 2009). If there is such a boundary, the Ca^{2+} signal would be sharply attenuated when crossing from the restricted dyad space into the bulk cytoplasm and back, reducing the chances of exciting the tetramers in the next dyad. Some of the multiclusters we found were very large, extending up to 1 µm (100 nm NL), 1.5 µm (150 nm NL), and nearly 2 µm on the application of ISO (150 nm NL, Fig. 6 B iv). It would seem unlikely that such large structures would act as a single CRU as is implied by the models. It is possible that, depending on the underlying dyad structure, a lower NL, 80 or 60 nm, could more accurately describe the properties of some multiclusters.

The relationship between tetramers and blinks with primary–secondary labeling

We found that our data generated a point cloud similar to that seen by Shen et al. (2019) to which we, as they did, fitted a straight line. Their equation has a slope less than a tenth of ours, indicating a much lower blinking rate, which might lead to incomplete reconstruction of the clusters and tetramers being missed. We established that our point cloud was real, not due to error, and that the area (tetramers) showed only a weak dependence on the number of blinks. A possible explanation for our result may lie in the nature of primary–secondary antibody binding, where both the number of bound monoclonal primaries per receptor and the number of polyclonal secondaries bound to those primaries is unknown. This results in an unknown number of fluorophores bound to each RyR2, a number highly unlikely to be constant. If we add the stochastic nature of fluorophore blinking, this produces a system that has a weak relationship between the number of blinks and the underlying proteins. We have only examined the relationship between blinking and area, and any relationship with the number of tetramers requires a correct (and constant) occupancy, which is currently uncertain.

The effects of phosphorylation

In two earlier papers (Asghari et al., 2014, 2020), our group showed that the tetramers within a dyad rearranged on phosphorylation as well as with the application of Mg^{2+} and the immunophilins FKBP12 and FKBP12.6. In this paper, we have shown that adding a physiologically appropriate concentration of ISO causes changes in the clusters within minutes of application.

Our results show that ISO causes a significant increase in cluster density, but we had to determine whether this was due to new clusters being created or the fragmentation of existing clusters. The number of subclusters per cluster for both the 100 and 150 nm NLs shows a significant increase, a change that has been associated with an increase in fragmentation in cells that are in atrial fibrillation (Macquaide et al., 2015) as well as those in heart failure (Kolstad et al., 2018). However, both studies used a metric that depended on the NL, and since the degree of fragmentation has to be a property of the cluster ensemble, we looked for a property of the base (30 nm NL) clusters rather than the groupings imposed by NLs greater than that. If we assume that an object that is broken into many small parts is more fragmented than one that has a few large parts, then a reduction in the former and an increase in the latter represents a decrease in fragmentation. This is exactly how the ISO distribution at the 30 nm NL changes compared with the control ($P = 2 \times 10^{-12}$; Table 1 and Fig. 5 C). The fragmentation of the clusters decreases with ISO, implying that the increase in cluster density is due to the movement of new tetramers into the jSR.

The decrease in fragmentation is associated with a significant increase in the size of the cluster areas, a decrease in the number of small clusters, and an increase in the number of medium-sized clusters (Fig. 5, A ii and B ii; and Fig. 6 B), suggesting that a number of small clusters are coalescing with larger ones, producing clusters that have a higher probability of producing a spark (Galice et al., 2018; Iaparov et al., 2021), assuming other parameters of the system are unchanged. The fitted ellipses around the clusters show that phosphorylation increases both axes, suggesting an overall swelling of the clusters. The decrease in edge-to-edge cluster distance (Table 5) could be due to the small clusters moving toward the large or the larger clusters expanding outward to engulf the small ones, or a combination of both. Resolving this requires real-time imaging of the effects of phosphorylation.

Does the tetramer density change?

ISO causes a 19% increase in the area that the clusters cover, partly due to the introduction of new clusters and partly because of the expansion of existing clusters. It is not clear whether the expansion causes a decrease in the density of the tetramers within the ISO-treated clusters or whether the introduction of new tetramers maintains the density at its original level. Modeling shows that such a decrease would decrease the excitability of the clusters (Iaparov et al., 2021), although that might be compensated for by phosphorylation-inducing changes in the gating properties of the RyR2. In our measurements of the occupancy of both control and ISO-treated clusters, we found no difference although, as we noted, these measurements were limited. Although density measurements within the myocyte interior found no change in phosphorylation (Asghari et al., 2020), we cannot exclude the possibility that the reduction of density due to the expansion of the clusters is not compensated for by the insertion of new tetramers into those clusters.

What causes cluster expansion?

Our group (Asghari et al., 2023 *Preprint*), using 2-D measurements of the dyad, have found that a phosphomimetic mutation of RyR2 (S2814D) as well as physiological doses of ISO significantly increased the size of the jSR, while in this paper, we have found that ISO causes the clusters to expand increasing their area. Since the RyR2 are embedded in the jSR, an obvious question is whether the two events are connected. The way in which the jSR expands is central to understanding what that interaction might be, as jSR expansion by accretion (i.e., adding to the periphery) or by coalescence (if it occurs) would not directly affect the dimension of the clusters, while expansion by addition or replacement might. If the jSR expands by accretion or coalescence, the changes in the jSR and the clusters would be independent of each other.

If jSR expansion is due to addition or replacement, the outcome will depend on whether the tetramers are actively (i.e., interacting with the jSR) or passively embedded. In case of the latter, the tetramers, single or in groups, would separate and move away from each other. That this does not happen is clear from the image of ISO-treated clusters in Fig. 3, B and C, where there are multiple clusters in which the tetramers are abutting each other. Further, Fig. 3 D shows a cluster with a central spine of interconnected tetramers, an arrangement impossible with passive movement and separation. In addition, tomographic data (Asghari et al., 2020) shows a small non-significant increase in the tetramer density on phosphorylation, contradicting the decrease predicted by a passive model of expansion.

The increase in the cluster density we found implies that tetramers are added in a dynamic process. A mechanism exists for this to occur; ISO is known to move phosphorylated RyR2 into BIN1 microdomains within the dyads (Fu et al., 2016). The jSR in mouse ventricular myocytes appears to be highly dynamic (Drum et al., 2020) with multiple dyads being formed and then dissipated within minutes; blocking of the motor proteins kinesin-1 and dynein greatly reduced the rate of appearance and disappearance. Combining these observations with the knowledge that phosphorylation of RyR2 appears to have a direct effect on the jSR enabled us to construct a hypothetical mechanism to explain the changes seen. We propose that the jSR movement observed by Drum et al. also transports tetramers to and from the jSR, with the rate of insertion and removal in quiescent cells cancelling out each other to reach a dynamic equilibrium or steady state. Further, we propose that phosphorylation of RyR2 changes the rates of insertion and removal, with insertion predominating, resulting in the introduction of both new tetramers and new clusters and expanding the jSR. This would explain the increased size of the clusters, the increased cluster density, and the jSR expansion. This effect could be achieved by an increase in the insertion rate, a decrease in the removal rate, or a combination of both. Eventually (but within minutes), a new steady

state will be achieved with the two rates in balance. We would predict that when phosphorylation is reduced to its basal level, the process would be reversed with the removal rate predominating, reducing the jSR and cluster size, tetramer number, and cluster density until the previous steady state is reached.

It is likely that the above mechanism is not the only way in which clusters may grow. We have noted a reduction in the number of small clusters on ISO treatment and suggested that this is due to the coalescence with other clusters. If the clusters are on the same portion of jSR, they could move toward each other; this does not have to be a large movement as about 10% of the clusters, constituting 20% of the total cluster area are between 30 and 40 nm apart (Table 3). It may be possible for two separate jSR to coalesce and the clusters on them to merge; however, Drum et al. (2020) observed jSR splitting rather than jSR coalescence, so if it occurs, it is probably a rare event.

In this model, where the RyR2 and the jSR actively interact, we do not know whether the jSR, in turn, has an effect on the RyR2, specifically on the rearrangement of the tetramers into different groupings that occurs with phosphorylation (Asghari et al., 2014, 2020). While there is evidence to suggest that it may not, as RyR2-S2814D shows no expansion of the jSR on ISO even though there is still a rearrangement of the tetramers (Asghari et al., 2023 *Preprint*), we cannot definitively say whether the mechanism that groups the tetramers in their array is separate from the one that governs cluster or jSR expansion.

Our two papers have found complementary results on the size of the clusters and the jSR, which has allowed us to construct a hypothesis to integrate them. In particular, we used two different methods of fixation; two separate methods of visualization, dSTORM and electron microscopy; two different areas of the myocyte, surface and interior; and different methods of analysis on two different species of rodent to arrive at a coherent model on the effects of phosphorylation.

The model of the mammalian ventricular dyad, common a decade ago, of a static RyR2 checkerboard array has been replaced by one in which the dyad and its associated RyR2 clusters are constantly rearranging and moving in response to stimuli.

Data availability

The full code for the analysis program is available in Zenodo at Scriven, 2023. This program can be compiled to run in either Windows or Linux. A Windows-compatible installation file RyR_STORM2D_Installer.exe is also available from GitHub at https://github.com/Dscriven/RyR_STORM2D, and can be used to install the program which can then read, display, and analyze the supplied blink data sets, openly available in Zenodo at Scriven et al. (2023). The data underlying the remaining figures (5–9) and the tables are openly available in the ClusterData zip file on Zenodo (Scriven et al., 2023).

Acknowledgments

David A. Eisner served as editor.

This study was partially funded by the Natural Sciences and Engineering Research Council of Canada (to K.C. Chou) and the Canada Foundation for Innovation (to K.C. Chou). E.D.W. Moore acknowledges a grant from CIHR (148527).

Author contributions: D.R.L. Scriven: conceptualization, software, investigation, formal analysis, data curation, validation, visualization, writing—original draft, and writing—review & editing. A.B. Johnsen: resources and investigation. P. Asghari: conceptualization, resources, and writing—review & editing. K.C. Chou: methodology, software, funding acquisition, and writing—review & editing. E.D.W. Moore: conceptualization, funding acquisition, supervision, writing—original draft, and writing—review & editing.

Disclosures: The authors declare no competing interests exist.

Submitted: 28 January 2022
Revised: 23 January 2023
Revised: 30 May 2023
Accepted: 2 September 2023

References

Asghari, P., D.R.L. Scriven, J. Hoskins, N. Fameli, C. van Breemen, and E.D.W. Moore. 2012. The structure and functioning of the couplon in the mammalian cardiomyocyte. *Protoplasma*. 249:S31–S38. https://doi.org/10.1007/s00709-011-0347-5

Asghari, P., D.R. Scriven, M. Ng, P. Panwar, K.C. Chou, F. van Petegem, and E.D. Moore. 2020. Cardiac ryanodine receptor distribution is dynamic and changed by auxiliary proteins and post-translational modification. *Elife*. 9:e51602. https://doi.org/10.7554/eLife.51602

Asghari, P., D.R.L. Scriven, S. Sanatani, S.K. Gandhi, A.I.M. Campbell, and E.D.W. Moore. 2014. Nonuniform and variable arrangements of ryanodine receptors within mammalian ventricular couplons. *Circ. Res.* 115: 252–262. https://doi.org/10.1161/CIRCRESAHA.115.303897

Asghari, P., D.R.L. Scriven, S. Shahrasebi, H.H. Valdivia, X.H.T. Wehrens, and E.D.W. Moore. 2023. Phosphorylation of RyR2 simultaneously expands the dyad and rearranges the tetramers. *bioRxiv*. https://doi.org/10.1101/2023.05.23.541024 (Preprint posted May 23, 2023)

Baddeley, D., I. Jayasinghe, L. Lam, S. Rossberger, M.B. Cannell, and C. Soeller. 2009. Optical single-channel resolution imaging of the ryanodine receptor distribution in rat cardiac myocytes. *Proc. Natl. Acad. Sci. USA*. 106:22275–22280. https://doi.org/10.1073/pnas.0908971106

Bernardini, F, and C L Bajaj. 1997. Sampling and reconstructing manifolds using alpha-shapes. *Department of Computer Science Technical Reports*. https://docs.lib.purdue.edu/cstech/1350

Bers, D.M. 2001. Excitation-Contraction Coupling and Cardiac Contractile Force. Second edition. Kluwer Academic Publishers, Dordrecht, Holland.

Breusch, T.S., and A.R. Pagan. 1979. A simple test for heteroscedasticity and random coefficient variation. *Econometrica*. 47:1287–1294. https://doi.org/10.2307/1911963

Cautun, M.C., and R. van de Weygaert. 2011. The DTFE public software: The delaunay tessellation field estimator code. arXiv. 10.48550/arXiv.1105.0370 (Preprint posted May 2, 2011)

Culley, S., D. Albrecht, C. Jacobs, P.M. Pereira, C. Leterrier, J. Mercer, and R. Henriques. 2018. Quantitative mapping and minimization of super-resolution optical imaging artifacts. *Nat. Methods*. 15:263–266. https://doi.org/10.1038/nmeth.4605

Drum, B.M., C. Yuan, A. de la Mata, N. Grainger, and L.F. Santana. 2020. Junctional sarcoplasmic reticulum motility in adult mouse ventricular myocytes. *Am. J. Physiol. Cell Physiol.* 318:C598–C604. https://doi.org/10.1152/ajpcell.00573.2019

Ferguson, D.G., H.W. Schwartz, and C. Franzini-Armstrong. 1984. Subunit structure of junctional feet in triads of skeletal muscle: A freeze-drying, rotary-shadowing study. *J. Cell Biol.* 99:1735–1742. https://doi.org/10.1083/jcb.99.5.1735

Fu, Y., S.A. Shaw, R. Naami, C.L. Vuong, W.A. Basheer, X. Guo, and T. Hong. 2016. Isoproterenol promotes rapid ryanodine receptor movement to bridging integrator 1 (BIN1)-organized dyads. *Circulation*. 133:388–397. https://doi.org/10.1161/CIRCULATIONAHA.115.018535

Galice, S., Y. Xie, Y. Yang, D. Sato, and D.M. Bers. 2018. Size matters: Ryanodine receptor cluster size affects arrhythmogenic sarcoplasmic reticulum calcium release. *J. Am. Heart Assoc.* 7:e008724. https://doi.org/10.1161/JAHA.118.008724

Gärtner, B., and S. Schönherr. 1998. Smallest enclosing ellipses: An exact and generic implementation. *Serie B – Informatik B 98-05, Freie Universität Berlin*. https://doi.org/ftp://ftp.inf.fu-berlin.de/pub/reports/tr-b-98-05.ps.gz

Hayashi, T., M.E. Martone, Z. Yu, A. Thor, M. Doi, M.J. Holst, M.H. Ellisman, and M. Hoshijima. 2009. Three-dimensional electron microscopy reveals new details of membrane systems for Ca^{2+} signaling in the heart. *J. Cell Sci.* 122:1005–1013. https://doi.org/10.1242/jcs.028175

Holm, S. 1979. A simple sequentially rejective multiple test procedure. *Scand. J. Stat. Theor. Appl.* 6:65–70.

Hou, Y., I. Jayasinghe, D.J. Crossman, D. Baddeley, and C. Soeller. 2015. Nanoscale analysis of ryanodine receptor clusters in dyadic couplings of rat cardiac myocytes. *J. Mol. Cell. Cardiol.* 80:45–55. https://doi.org/10.1016/j.yjmcc.2014.12.013

Huang, F., S.L. Schwartz, J.M. Byars, and K.A. Lidke. 2011. Simultaneous multiple-emitter fitting for single molecule super-resolution imaging. *Biomed. Opt. Express*. 2:1377–1393. https://doi.org/10.1364/BOE.2.001377

Iaparov, B.I., I. Zahradnik, A.S. Moskvin, and A. Zahradníková. 2021. In silico simulations reveal that RYR distribution affects the dynamics of calcium release in cardiac myocytes. *J. Gen. Physiol.* 153:e202012685. https://doi.org/10.1085/jgp.202012685

Jayasinghe, I., A.H. Clowsley, R. Lin, T. Lutz, C. Harrison, E. Green, D. Baddeley, L. Di Michele, and C. Soeller. 2018. True molecular scale visualization of variable clustering properties of ryanodine receptors. *Cell Rep.* 22:557–567. https://doi.org/10.1016/j.celrep.2017.12.045

Kolstad, T.R., J. van den Brink, N. MacQuaide, P.K. Lunde, M. Frisk, J.M. Aronsen, E.S. Norden, A. Cataliotti, I. Sjaastad, O.M. Sejersted, et al. 2018. Ryanodine receptor dispersion disrupts Ca^{2+} release in failing cardiac myocytes. *Elife*. 7:e39427. https://doi.org/10.7554/eLife.39427

Macquaide, N., H.T.M. Tuan, J.I. Hotta, W. Sempels, I. Lenaerts, P. Holemans, J. Hofkens, M.S. Jafri, R. Willems, and K.R. Sipido. 2015. Ryanodine receptor cluster fragmentation and redistribution in persistent atrial fibrillation enhance calcium release. *Cardiovasc. Res.* 108:387–398. https://doi.org/10.1093/cvr/cvv231

Novotová, M., A. Zahradníková Jr, Z. Nichtová, R. Kováč, E. Kráľová, T. Stankovičová, A. Zahradníková, and I. Zahradník. 2020. Structural variability of dyads relates to calcium release in rat ventricular myocytes. *Sci. Rep.* 10:8076. https://doi.org/10.1038/s41598-020-64840-5

Scholz, F.W., and M.A. Stephens. 1987. K-sample anderson-darling tests. *J. Am. Stat. Assoc.* 82:918–924. https://doi.org/10.2307/2288805

Scriven, D.R.L. 2023. RyR_STORM2D (1.3.1). *Zenodo*. https://doi.org/10.5281/zenodo.7919290

Scriven, D.R.L., A. Klimek, K.L. Lee, and E.D.W. Moore. 2002. The molecular architecture of calcium microdomains in rat cardiomyocytes. *Ann. N. Y. Acad. Sci.* 976:488–499. https://doi.org/10.1111/j.1749-6632.2002.tb04783.x

Scriven, D.R.L., A.B. Johnsen, P. Asghari, K.C. Chou, and E.D.W. Moore. 2023. Cardiomyocyte ryanodine receptor clusters expand and coalesce after application of isoproterenol. *Zenodo*. https://doi.org/10.5281/zenodo.8271651

Shen, X., J. van den Brink, Y. Hou, D. Colli, C. Le, T.R. Kolstad, N. MacQuaide, C.R. Carlson, P.M. Kekenes-Huskey, A.G. Edwards, et al. 2019. 3D dSTORM imaging reveals novel detail of ryanodine receptor localization in rat cardiac myocytes. *J. Physiol.* 597:399–418. https://doi.org/10.1113/JP277360

Sobie, E.A., S. Guatimosim, L. Gómez-Viquez, L.S. Song, H. Hartmann, M. Saleet Jafri, and W.J. Lederer. 2006. The Ca^{2+} leak paradox and rogue ryanodine receptors: SR Ca^{2+} efflux theory and practice. *Prog. Biophys. Mol. Biol.* 90:172–185. https://doi.org/10.1016/j.pbiomolbio.2005.06.010

Tafteh, R., D.R.L. Scriven, E.D.W. Moore, and K.C. Chou. 2016. Single molecule localization deep within thick cells; a novel super-resolution microscope. *J. Biophotonics*. 9:155–160. https://doi.org/10.1002/jbio.201500140

Van Petegem, F. 2015. Ryanodine receptors: Allosteric ion channel giants. *J. Mol. Biol.* 427:31–53. https://doi.org/10.1016/j.jmb.2014.08.004

Wong, B. 2011. Color blindness. *Nat. Methods*. 8:441. https://doi.org/10.1038/nmeth.1618

Yin, C.C., H. Han, R. Wei, and F.A. Lai. 2005. Two-dimensional crystallization of the ryanodine receptor Ca^{2+} release channel on lipid membranes. *J. Struct. Biol.* 149:219–224. https://doi.org/10.1016/j.jsb.2004.10.008

Yin, C.C., and F.A. Lai. 2000. Intrinsic lattice formation by the ryanodine receptor calcium-release channel. *Nat. Cell Biol.* 2:669–671. https://doi.org/10.1038/35023625

Supplemental material

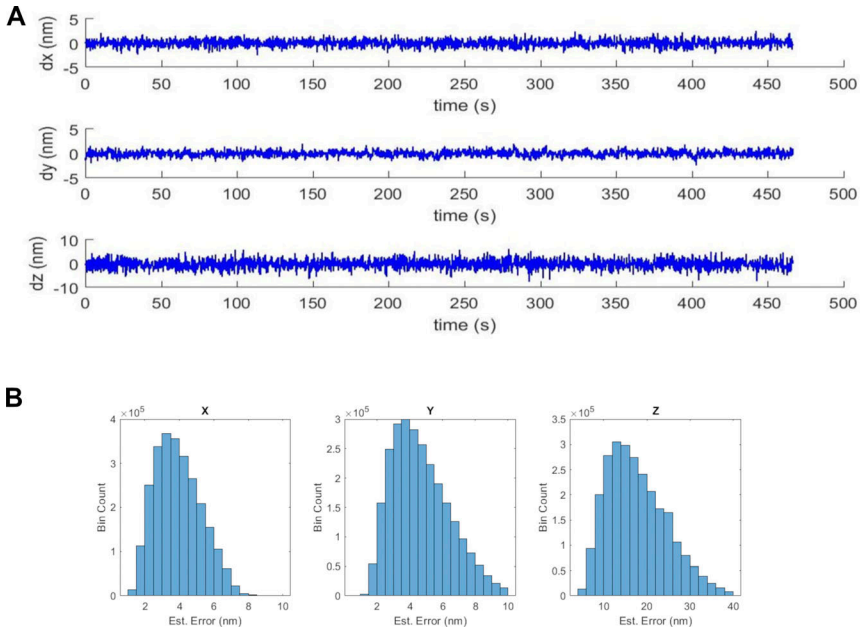

Figure S1. **Imaging system parameters. (A)** Stability of the x, y, and z axes of the piezoelectric stage for the duration of a single image acquisition. **(B)** Estimated errors in the positioning of the x, y, and z values for 2.6×10^6 control blinks.

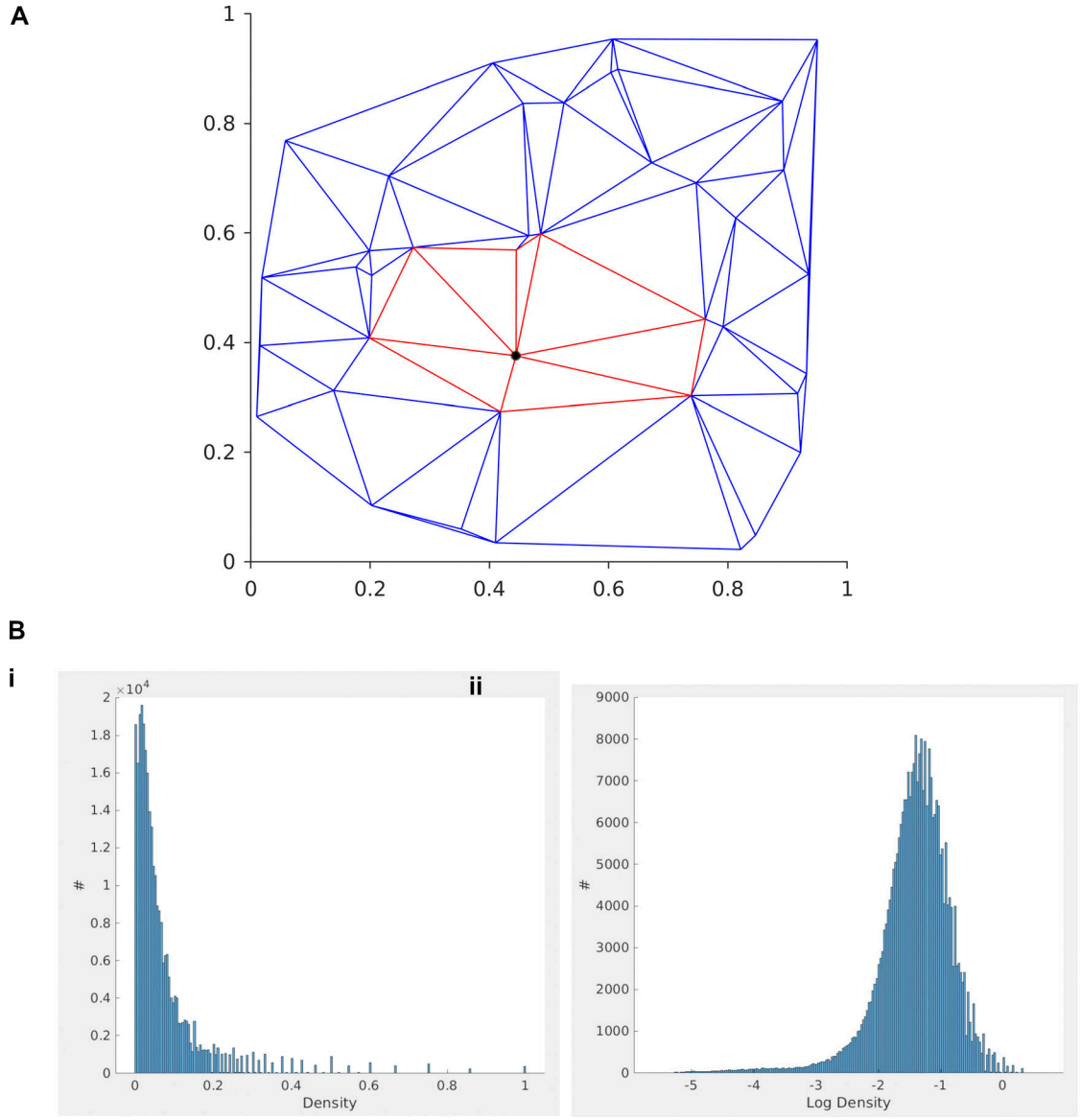

Figure S2. **Calculating the blink density. (A)** An arbitrary set of points with a Delaunay triangulation (blue). The density of the black point is given by the reciprocal of the sum of the areas in red. If there is more than one blink at a point, the density is multiplied by the number of blinks. **(B i and ii)** Histogram of blink density plotted on a linear (i) and logarithmic (ii) scale. The data is from a cell, a surface segment of which is displayed in Fig. 1 A.

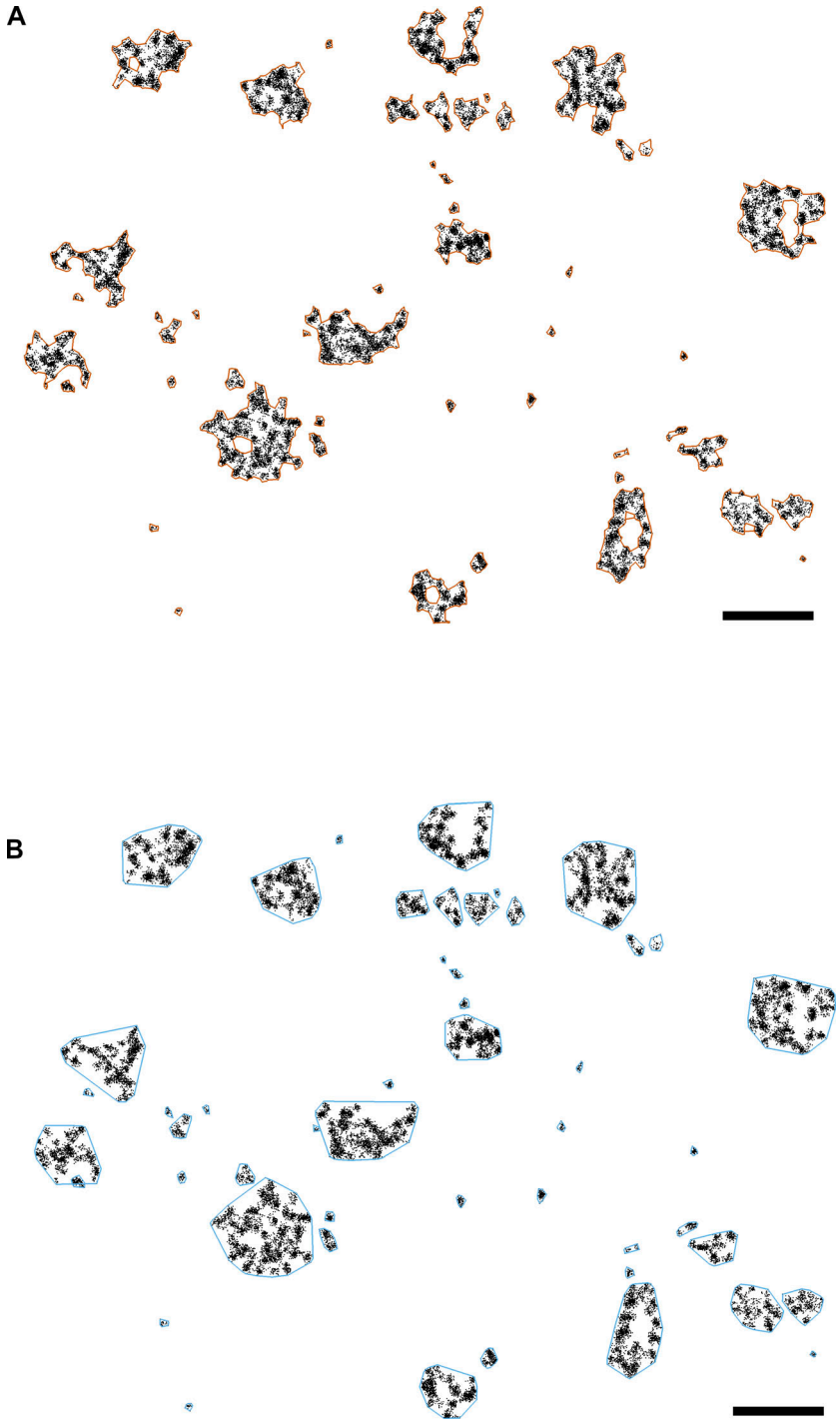

Figure S3. **Examples of α-shapes and minimum ellipses. (A)** Control cell (Fig. 1 B) showing the α-shape generated boundaries (vermillion) of each cluster. Scale bar, 500 nm. **(B)** Control cell (Fig. 1 B) showing fitted ellipses (sky blue). Neighborhood limit was 50 nm. Scale bar, 500 nm.

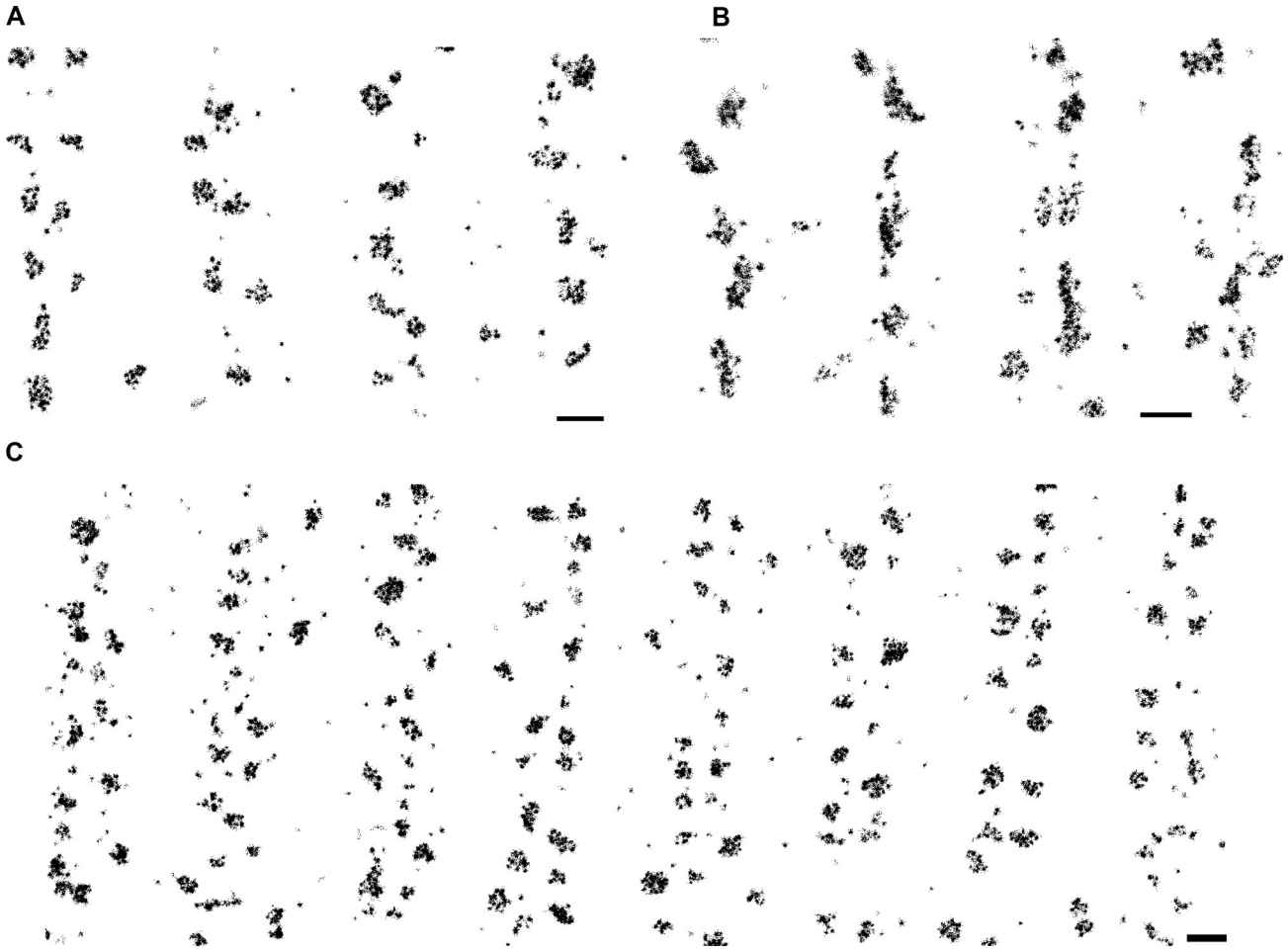

Figure S4. **Control cell blink distribution. (A–C)** Clusters showing tetramers on the surface of three different control cells. Note the large variation in size, shape, and density of the clusters. Scale bars, 500 nm.

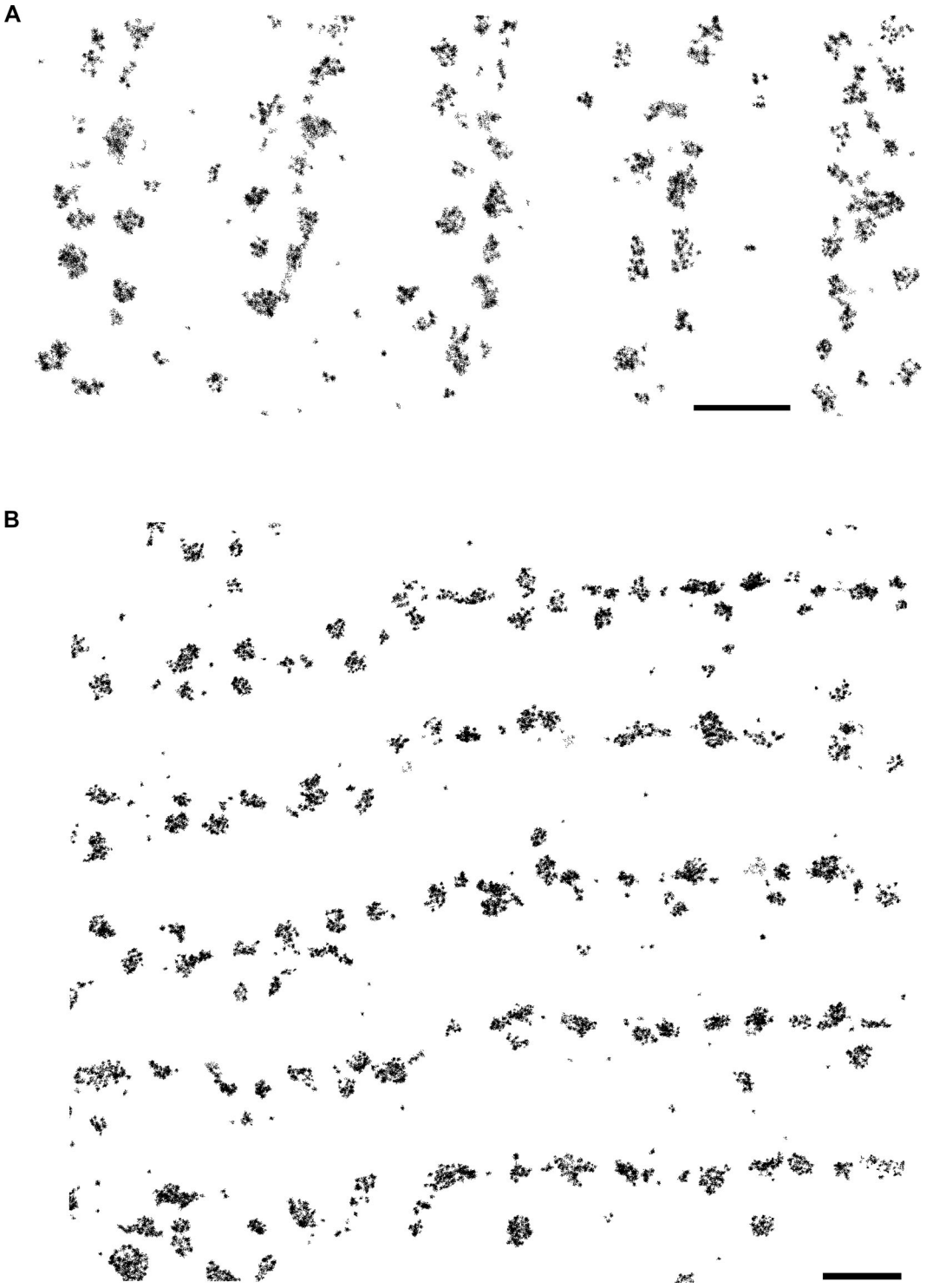

Figure S5. **Blink distribution in phosphorylated cells. (A and B)** Blink data showing the effect of 300 nmol/liter ISO on the surface distribution of clusters in two different cells. Scale bar, 1 µm.